International Journal of Multiphase Flow 202 (2026) 105844

Contents lists available at ScienceDirect

International Journal of Multiphase Flow

journal homepage: www.elsevier.com/locate/ijmulflow

Research Paper

A dynamic framework for simulating cavitation inception with Large Eddy Simulation

Mehedi H. Bappy [a], Krishnan Mahesh [a,b,c,*]

[a] Center for Naval Research & Education, Naval Architecture and Marine Engineering, University of Michigan, Ann Arbor, 48105, MI, USA
[b] Mechanical Engineering, University of Michigan, Ann Arbor, 48109, MI, USA
[c] Aerospace Engineering, University of Michigan, Ann Arbor, 48109, MI, USA

ARTICLE INFO

Keywords:
Cavitation inception
SGS modeling
Vortex–vortex interaction

ABSTRACT

We present a Large Eddy Simulation (LES) model that dynamically computes all variables critical to cavitation inception. Cavitation onset is determined not only by resolved flow features and their interaction, but also by rare, extreme low-pressure events driven by unresolved turbulence. Recent work by Madabhushi and Mahesh (2026) demonstrates that capturing the pressure minima responsible for inception requires extremely fine computational grids. Our approach addresses this limitation by incorporating a dynamic k-equation SGS closure, a statistical SGS cavitation inception model that utilizes local pressure fluctuations, and a vapor transport equation for dynamic variation in nuclei density. We applied the model to a canonical twin vortex configuration, using multiple grid resolutions and a range of angles of attack (AOA), both with and without dynamic nuclei distributions. The framework accurately predicted both the inception location and reference pressure, showing close agreement with experimental measurements across all grids and AOAs. Notably, the model reliably captured inception events even when resolved pressures alone would underestimate inception probability. This validation demonstrates the predictive capability and suitability of the framework for engineering simulation of cavitation onset in turbulent flows while maintaining practical computational efficiency.

1. Introduction

Cavitation refers to the formation and subsequent dynamic evolution of vapor-filled cavities within a liquid subjected to sufficiently low local pressures. Its occurrence is pervasive across several engineering disciplines where it can negatively impact system performance, structural integrity, and operational longevity (Brennen, 2014; Knapp et al., 1970). In marine applications, cavitation on propeller blades or control surfaces can lead to a marked reduction in propulsive efficiency, induce severe erosive damage, generate unwanted vibrations, and significantly amplify radiated underwater noise (Smith et al., 2024). Predicting the conditions leading to cavitation inception — the initial formation of these vaporous bubbles — is therefore important for the design of robust and reliable systems.

The fundamental physics governing cavitation inception relies on the local fluid pressure, p, the liquid's vapor pressure, p_v, and the availability of nucleation sites. Cavitation typically occurs when the local pressure in the liquid drops below its vapor pressure at a given temperature. This pressure reduction can be induced by high local velocities, such as those encountered in regions of flow acceleration around hydrofoils, within pump impellers, or in the cores of intense vortical structures. The susceptibility of a flow to cavitation is often quantified by the cavitation number, σ, defined as:

$$\sigma = \frac{p_\infty - p_v}{\frac{1}{2}\rho U_\infty^2} \tag{1}$$

where p_∞ is the reference far-field pressure, U_∞ is a reference velocity, and ρ is the liquid density (Brennen, 2014). A lower cavitation number indicates a greater propensity for cavitation.

Cavitation inception is intimately linked to the dynamics of vortical structures. Shear-dominated flows, such as those developing in the wake of hydrofoils, around propellers, or within mixing layers, are inherently characterized by the formation, evolution, and interaction of vortices. These vortices, defined by regions of concentrated vorticity often exhibit significantly reduced pressures within their cores providing a natural locus for cavitation inception (Saffman, 1992). The work of Harvey et al. (1947) highlighted the importance of pre-existing gas nuclei stabilized in crevices for heterogeneous nucleation. Subsequent experimental investigations by numerous researchers further elucidated the link between flow separation, vortex formation, and cavitation inception on various body shapes, see Morch (2000).

* Corresponding author.
E-mail address: krmahesh@umich.edu (K. Mahesh).

https://doi.org/10.1016/j.ijmultiphaseflow.2026.105844
Received 23 February 2026; Received in revised form 1 May 2026; Accepted 9 July 2026
Available online 16 July 2026

A particularly complex and challenging scenario arises from the three-dimensional interaction of multiple vortical structures. In flows such as those around marine propellers and control surfaces, cavitation inception is frequently observed not within the primary, often spanwise-oriented, shedding vortices, but rather within weaker, typically streamwise or obliquely oriented, secondary vortical structures. Experimental observations and numerical simulations show that the intense strain field imposed by stronger, primary vortices can induce significant stretching of these weaker, secondary vortices (Knister, 2024; Leasca et al., 2025). The stretching process, by conserving angular momentum within the vortex core, leads to an amplification of vorticity and a concurrent reduction in core size, resulting in a dramatic decrease in core pressure, often sufficient to trigger cavitation even when the ambient cavitation number is relatively high (Tennekes and Lumley, 1972). Furthermore, the inherent instabilities present in turbulent shear flows can enhance these vortex interactions and transient pressure minima. Long-wavelength instabilities, such as the Crow instability observed in systems of counter-rotating vortices (Crow, 1970), can lead to significant mutual distortion, stretching, and eventual reconnection or merging of vortical structures. These dynamic events create localized, transient regions of exceptionally low pressure within the cores of the interacting, often weaker, vortices, making them prime candidates for cavitation inception. Observations by Chang et al. (2012) and recent advanced experimental investigations, such as those by Knister et al. (2020) and Knister (2024), employing sophisticated techniques like stereoscopic Particle Image Velocimetry (PIV) coupled with high-speed cavitation visualization, show the intricate three-dimensional kinematics and dynamics of these interacting vortex systems and their direct correlation with incipient cavitation events.

Predictive modeling of cavitation inception, particularly in complex three-dimensional and turbulent flow fields, remains a formidable challenge. Cavitation inception is inherently a multi-scale process, driven by transient, extreme pressure minima that occur within the smallest turbulent eddies. Accurately capturing these short-lived, localized events poses a significant challenge for numerical simulations, as demonstrated by Madabhushi and Mahesh (2026), which highlights that reliable prediction of cavitation inception in twin vortex interactions undergoing Crow instability, requires simulations with very fine spatial and temporal resolution. Direct Numerical Simulation (DNS), while capable of resolving all relevant turbulent scales and the associated pressure fluctuations, remains computationally prohibitive for the high Reynolds number flows characteristic of practical engineering applications. Reynolds-Averaged Navier–Stokes (RANS) models, fundamentally rely on time-averaging the flow equations. This averaging process inherently smooths out the transient, small-scale pressure fluctuations that are the primary triggers for cavitation inception. LES explicitly resolves large, energy-containing turbulent eddies while modeling only smaller, SGS motions. LES has demonstrated its potential to capture the unsteady dynamics of sheet, cloud, and vortex cavitation (Gnanaskandan and Mahesh, 2015) , but accurately predicting inception remains a challenge (Madabhushi and Mahesh, 2026; Bappy, 2022). The most critical extreme pressure minima frequently manifest at the unresolved subgrid scales, which are effectively ignored or inadequately represented by standard LES closures. The resolved pressure field obtained from LES, $\bar{p}$, may not accurately represent the instantaneous local pressure, p, experienced by a cavitation nucleus. Although traditional LES approaches transport of resolved vapor structures, they do not incorporate a mechanism for stochastic inception events that arise from unresolved turbulence. This necessitates the development and implementation of a dynamic LES framework that aims to account for the influence of unresolved pressure fluctuations, $p'_{sgs} = p - \bar{p}$, and their impact on the activation of cavitation nuclei.

1.1. Overview of the proposed LES framework

We propose a novel LES framework that has the following key components.

1. Dynamic SGS Turbulent Kinetic Energy Model (Chai and Mahesh, 2012): This dynamic one-equation model solves a transport equation for the SGS turbulent kinetic energy, k_{sgs}. This provides a dynamic and physically consistent measure of unresolved turbulence and its fluctuations, which are essential inputs for the SGS cavitation model.
2. SGS Cavitation Event Rate Model (Bappy et al., 2022): This model statistically accounts for unresolved pressure fluctuations at the subgrid level, effectively bypassing the strict requirement for extremely high spatial and temporal resolution. It allows for accurate cavitation inception predictions on coarser computational grids by relating the probability of an inception event to the local subgrid flow conditions.
3. Dynamic Nuclei Transport Model (Brandao and Mahesh, 2022): Another aspect of the current approach is the utilization of a vapor transport model, which enables the dynamic computation of void fraction and the handling of polydisperse nuclei size distributions. This component is vital for accurately representing the sensitive dependence of cavitation inception on water quality and local nuclei concentration in highly turbulent flows, as nuclei can be convected, trapped in vortical structures, or generated by previous cavitation events.

The synergy between these models is central to achieving both accuracy and computational efficiency. The dynamic SGS turbulent kinetic energy provides the local turbulent environment, which then informs the statistical cavitation model, while the dynamic nuclei transport provides "seed" population for cavitation. The remainder of this paper is organized as follows. Section 2 details the LES governing equations, the dynamic k_{sgs} and nuclei transport models along with the SGS cavitation inception model, and the numerical setup for the investigated flow configurations. Section 3 presents the results of our simulations, focusing on the vortex dynamics, pressure field characteristics, and predicted cavitation inception behavior under various conditions, including analyses of grid and nuclei sensitivity.

2. Methodology

This section discusses the governing equations, the SGS closure for the momentum equations, the statistical model employed for predicting cavitation inception, and the dynamic model for nuclei concentration.

2.1. Governing equations for LES

The simulations are performed using an unstructured overset grid method (Horne and Mahesh, 2021), which allows for increased flexibility by enabling meshes to overlap and move relative to each other. This approach provides fine resolution in key areas while coarsening away from those regions, which significantly reduces the total cell count and computational cost. The governing equations for the resolved-scale fluid motion are given by the filtered continuity equation:

$$\frac{\partial \bar{u}_i}{\partial x_i} = 0 \tag{2}$$

and the filtered momentum equation:

$$\frac{\partial \bar{u}_i}{\partial t} + \frac{\partial (\bar{u}_i \bar{u}_j)}{\partial x_j} = -\frac{1}{\rho}\frac{\partial \bar{p}}{\partial x_i} + \nu \frac{\partial^2 \bar{u}_i}{\partial x_j \partial x_j} - \frac{\partial \tau_{ij}}{\partial x_j}. \tag{3}$$

Here, x_i represents the Cartesian coordinates ($i = 1, 2, 3$), t is time, u_i is the ith component of the filtered velocity vector, ρ is the constant fluid density, $\bar{p}$ is the filtered pressure, and ν is the kinematic viscosity of the fluid. The overbar $(\bar{\cdot})$ denotes the spatial filtering operation.

The term τ_{ij} in Eq. (3) is the SGS stress tensor, which arises from the filtering operation and represents the effect of the unresolved small-scale motions on the resolved large scales. This tensor is unclosed and requires modeling, it is defined as:

$$\tau_{ij} = \overline{u_i u_j} - \bar{u}_i \bar{u}_j \tag{4}$$

Eq. (3) is solved using a finite volume segregated predictor–corrector scheme. The velocities are first predicted by solving the momentum equation and then corrected using the pressure Poisson equation to satisfy the continuity equation. The implicit Crank–Nicolson scheme is used for the temporal advancement of the solution. The interpolation between centroid and face velocities is performed in a manner that emphasizes discrete kinetic energy conservation.

2.2. Dynamic k-equation SGS model (DkM)

To close Eq. (3), the SGS stress tensor τ_{ij} modeled using an eddy viscosity approach. The deviatoric part of the SGS stress tensor, $\tau_{ij}^d = \tau_{ij} - \frac{1}{3}\tau_{kk}\delta_{ij}$(where τ_{kk} is the trace of the SGS stress tensor, representing twice the SGS turbulent kinetic energy k_{sgs}, and δ_{ij} is the Kronecker delta), is related to the resolved rate-of-strain tensor $\overline{S}_{ij}$:

$$\tau_{ij}^d = -2\nu_{\mathrm{sgs}}\bar{S}_{ij} = -2\nu_{\mathrm{sgs}}\left(\frac{1}{2}\left(\frac{\partial \bar{u}_i}{\partial x_j} + \frac{\partial \bar{u}_j}{\partial x_i}\right)\right) \tag{5}$$

where ν_{sgs} is the SGS eddy viscosity.

In this work, ν_{sgs} is determined using a dynamic one-equation model based on the transport of SGS turbulent kinetic energy, $k_{\mathrm{sgs}} = \frac{1}{2}\tau_{kk}$. We employ the model proposed by Chai and Mahesh (2012) where the SGS stress tensor is defined by the following relation, where $\sqrt{k}$ is chosen as the velocity scale instead of $\Delta|\overline{S}|$:

$$\tau_{ij} - \frac{2}{3}\rho k \delta_{ij} = -2C_S \Delta \rho \sqrt{k}\bar{S}_{ij}^*. \tag{6}$$

Here, C_S is the model coefficient for SGS stress and S_{ij}^* is the traceless strain-rate tensor defined as -

$$\tilde{S_{ij}^*} = \tilde{S_{ij}} - \frac{1}{3}\delta_{ij}\tilde{S_{kk}} = \frac{1}{2}\left(\frac{\partial \bar{u}_i}{\partial x_j} + \frac{\partial \bar{u}_j}{\partial x_i}\right) - \frac{1}{3}\frac{\partial \bar{u}_k}{\partial x_k}\delta_{ij}. \tag{7}$$

A key feature of the model used is the dynamic determination of model coefficients in the k_{sgs}-equation. This dynamic procedure adapts the model to the local state of the flow, alleviating the need for ad-hoc tuning of constants. The approach typically involves the application of a second, test filter (with width $\hat{\Delta} > \Delta$) to the resolved flow field, allowing for the evaluation of Germano-type identities for k_{sgs} or related quantities (Germano et al., 1991; Lilly, 1992). The Lagrangian time scale is dynamically computed based on a surrogate-correlation of the Germano-identity error (Verma et al., 2013). This methodology aims to provide a more robust estimation of the SGS dissipation and viscosity. Note that, we are using the incompressible *DkM* while Chai and Mahesh (2012) used the compressible *DkM* in their study .

2.3. SGS cavitation inception model

The dynamic SGS framework relies on local turbulence properties, extracted via the dynamic k_{sgs} transport model. k_{sgs} sets the scale for unresolved, rapid fluctuations in the pressure field. SGS velocity fluctuation (u'_{sgs}) gives the RMS of the unresolved velocity field and is defined as -

$$u'_{\mathrm{sgs}} = \sqrt{\frac{2}{3}k_{\mathrm{sgs}}}. \tag{8}$$

SGS Taylor-scale Reynolds Number (Re_{sgs}) is computed as:

$$Re_{\mathrm{sgs}} = \frac{u'_{\mathrm{sgs}}\lambda}{\nu} = \frac{2.58k_{\mathrm{sgs}}}{\sqrt{\nu\epsilon_{\mathrm{sgs}}}}, \tag{9}$$

where λ is the Taylor microscale ($= \sqrt{\frac{15\nu u'^2_{\mathrm{sgs}}}{\epsilon_{\mathrm{sgs}}}}$), and ϵ_{sgs} is the local SGS dissipation rate. ϵ_{sgs} is modeled in terms of the cell filter width Δ and the resolved strain rate S:

$$\epsilon_{\mathrm{sgs}} = (C_s\Delta)^2 S^3. \tag{10}$$

Cavitation inception for a nucleus of equilibrium radius R_0 occurs when the instantaneous local pressure $p = \bar{p} + p'_{\mathrm{sgs}}$ drops below a critical threshold, p_{crit}. This threshold is set by the Blake criterion, encapsulating vapor pressure, surface tension, and the effects of non-condensable gas:

$$p_{\mathrm{crit}}(R_0) = p_v - \frac{2S}{R_0} + p_g(R_0), \tag{11}$$

where p_v is vapor pressure, S surface tension, and p_g the partial pressure of non-condensable gas inside the nucleus (Brennen, 2014). Under isothermal expansion, gas pressure evolves as:

$$p_g = p_{g0}\left(\frac{R_0}{R}\right)^3, \tag{12}$$

with p_{g0} the initial gas pressure at R_0, and R instantaneous bubble radius. SGS pressure fluctuations, p'_{sgs}, can intermittently trigger inception even if $\bar{p}$ remains above threshold and requires a statistical treatment since LES only resolves the filtered pressure $\bar{p}$.

Beyond a simple pressure threshold, "detectable" cavitation requires sufficient residence time below p_{crit} for the nucleus to grow. To account for these temporal scales, we use a precomputed database that maps the local SGS state to probabilistic cavitation event frequencies, f_{cav} (Bappy et al., 2022). This cavitation event rate is determined using a subgrid-scale framework that connects the gap between resolved flow scales and microscale bubble dynamics. The bubble dynamics are accounted for a posteriori through a precomputed database. This database was constructed by solving the Rayleigh–Plesset equation for a vast ensemble of nuclei subjected to stochastic pressure histories derived from DNS of homogeneous isotropic turbulence (HIT). This a posteriori coupling ensures that the extreme, high-frequency pressure excursions — which occur at timescales much smaller than the LES timestep — are physically represented without the prohibitive cost of a fully coupled bubble-tracking simulation. By utilizing a 4D interpolant f_{db4}, the local cavitation event rate per nuclei is determined based on the resolved and subgrid pressure fields for every grid cell:

$$f_{\mathrm{cav}}(\mathbf{x}, t) = f_{db4}(Re_\lambda, \epsilon_{\mathrm{sgs}}, R_0, p_{\mathrm{abs}}) \tag{13}$$

Here, p_{abs} represents the total local absolute pressure used for inception evaluation, combining resolved and modeled subgrid-scale contributions. In our LES framework, this is defined as:

$$p_{\mathrm{abs}} = p_{\mathrm{ref}} + (\bar{p} + p'_{\mathrm{sgs}})\,\rho U_\infty^2, \tag{14}$$

where $\bar{p}$ is the non-dimensional resolved pressure obtained directly from the LES solver, and p'_{sgs} is the non-dimensional SGS pressure-fluctuation contribution (this is used only for inception/event-rate evaluation and does not modify the LES-resolved pressure field). Consistent with pressure–velocity scaling for locally isotropic unresolved turbulence, the characteristic SGS pressure scale satisfies $p'_{\mathrm{sgs}}\rho U_\infty^2 \sim \rho k_{sgs}$ (i.e., $p'_{\mathrm{sgs}} \sim k_{sgs}/U_\infty^2$), and the statistics of these SGS excursions are represented using the HIT-based database. To match the pressure between numerical and experimental conditions, p_{ref} represents the static pressure at the reference location.

To obtain the total cavitation event rate for a defined p_{ref}, f_{cav} is integrated over the computational volume, time, and the distributed population of nuclei:

$$F_{\mathrm{cav}}(p_{ref}) = \int_0^T \int_V \int_{R_0} f_{cav}(\mathbf{x}, t)\; N(R_0)\, dR_0\, dV\, dt \tag{15}$$

Here, $N(R_0)$ represents the nuclei size distribution. The time-averaged event rate is given by:

$$\overline{F}_{\mathrm{cav}}(p_{ref}) = \frac{F_{\mathrm{cav}}(p_{ref})}{T} \tag{16}$$

This modeling approach is specifically designed for the incipient regime where nuclei are dilute.

2.4. Dynamic nuclei concentration model

Physically consistent modeling of cavitation inception depends on capturing the dynamic evolution of nuclei concentrations and their size distributions. In turbulent flows, the number and size of nuclei are rarely spatially uniform or temporally constant, as they are influenced by advection, turbulent diffusion, local recirculation, and pressure fluctuations (Katz, 1984). To capture these dynamics, we utilize an incompressible single-phase formulation for the liquid carrier phase. This approach is physically justified by the fact that during the incipient regime, the void fractions are sufficiently low that the flow may be treated as a pure liquid with a dilute secondary phase. We employ a dynamic model that evolves nuclei concentration as a function of the local flow variables. While Euler–Lagrange methods provide high fidelity by tracking individual bubble trajectories, they become computationally prohibitive in large-scale interactions where tracking millions of discrete nuclei might be required (Mathai et al., 2020; Cheng et al., 2021). A statistical framework offers a computationally efficient alternative by treating the nuclei population as a continuous scalar field, making it better suited for high-Reynolds-number turbulent interactions while still capturing the essential physics of nuclei redistribution. The nuclei population is characterized by a size distribution $N(R_0, \vec{x}, t)$, where $N(R_0)$ denotes the number density of nuclei (per unit volume per unit radius interval) at location $\vec{x}$ and time t. The total local vapor volume fraction (α) occupied by nuclei is

$$\alpha(\vec{x}, t) = \int_{R_{min}}^{R_{max}} \frac{4}{3}\pi R_0^3 N(R_0, \vec{x}, t), \mathrm{d}R_0. \tag{17}$$

The vapor concentration C is related to the local vapor volume fraction such that

$$C(\vec{x}, t) = \alpha(\vec{x}, t) \cdot \rho_v. \tag{18}$$

For practical implementation within LES, we solve a scalar transport equation for the vapor concentration:

$$\frac{\partial C}{\partial t} + \frac{\partial}{\partial x_j}(\overline{u_j} C) = \frac{\partial}{\partial x_j}(D_C \frac{\partial C}{\partial x_j}) + \frac{\partial \tau_s}{\partial x_j} + S_e - S_c \tag{19}$$

where D_C is the nuclei diffusivity, which depends on local turbulence through a turbulent Schmidt number $Sc_t = (\nu + \nu_{\mathrm{sgs}})/D_C$. And the SGS scalar flux term $\tau_s = \overline{Cu_j} - \bar{C}\bar{u}_j$ is computed similarly as Eq. (4).

The source and sink terms, S_e and S_c, represent the local rate of change in vapor concentration due to cavitation processes (evaporation and condensation, respectively). These are formulated as:

$$S_e = C_e \overline{\alpha^2}(1-\overline{\alpha})^2 \frac{\rho_l}{\rho_v} \frac{\max(p_v - \overline{p}, 0)}{\sqrt{2\pi R_v T}} \tag{20}$$

$$S_c = C_c \overline{\alpha^2}(1-\overline{\alpha})^2 \frac{\max(\overline{p} - p_v, 0)}{\sqrt{2\pi R_v T}} \tag{21}$$

where C_e, C_c are constants, $\overline{\alpha}$ is the vapor volume fraction, ρ_l and ρ_v are the liquid and vapor densities, p_v is the vapor pressure, $\overline{p}$ is the filtered pressure, R_v is the gas constant for vapor, and T is temperature. These terms ensure that the model captures the generation and removal of vapor due to cavitation. The dynamic vapor concentration field $C(\vec{x}, t)$ thus serves as a locally resolved input for the SGS cavitation inception model, ensuring that predictions of cavitation onset reflect the true, inhomogeneous distribution of vapor in the flow. Implementation details of the vapor transport model is discussed in Brandao and Mahesh (2022).

In a fully polydisperse framework, Eq. (19) can be generalized and solved for each nuclei size class to track $N(R_0, \vec{x}, t)$, providing maximum resolution for multi-scale or population balance applications. For the monodisperse-approach presented here, $C(R_0) \propto N(R_0)$, and

$$N(R_0)_{t=t_n} = \frac{N(R_0)_{t=0} \cdot C(R_0)_{t=t_n}}{C(R_0)_{t=0}}. \tag{22}$$

3. Numerical setup

This study investigates cavitation inception due to the interaction of vortices generated by a twin hydrofoil flow configuration under the same conditions as the experiments of Knister (2024). It involves a pair of hydrofoils, fixed at certain AOAs, designed to generate unequal strength vortex pairs that interact with each other downstream of the foils, providing a canonical setup for studying vortex-induced cavitation inception mechanisms. This configuration is designed to create a controlled environment in which a weaker stream-wise vortex is subjected to the strain field of a stronger primary vortex, leading to stretching and intensification of the weaker vortex core.

The hydrofoils are based on a modified NACA 66 section, same as those used by Knister (2024). Both hydrofoils have a root chord length $c = 167$ mm. The primary (bottom) hydrofoil is a rectangular planform with the modified NACA 66 profile, set at an AOA of 6° relative to the incoming flow. This foil is designed to generate a relatively strong tip vortex. The secondary (top) hydrofoil, responsible for generating the weaker vortex that is targeted for cavitation inception, features the same modified NACA 66 profile but is tapered along its span and has a curved tip. This geometry promotes the formation of a more concentrated, tightly rolled-up tip vortex. This foil is mounted upstream and above the primary foil and is set at different AOAs of 0°, −2°, −4° (N0, N2, and N4). The relative positioning of the foils is critical to achieve the desired vortex interaction. Fig. 1 illustrates the numerical setup, detailing the hydrofoil geometries, their relative spacing, and orientation within the computational domain. Details of the hydrofoils and test section design can be found in Knister (2024).

The computational domain is a rectangular channel. The leading edge is at $x = 0$ and the trailing edge is at $x = 1.0$. The domain extends $2c$ upstream of the leading edge of the primary hydrofoil, $5c$ downstream to allow full development and observation of the interacting vortices, and $0.65c$ in the vertical and $0.63c$ in the spanwise directions from the center of the hydrofoil system. A uniform velocity profile $\mathbf{u} = (U_\infty, 0, 0)$ with $U_\infty = 10$ m/s is specified at the inlet while an outflow boundary condition with zero-gradient velocity and pressure applied at the outlet. No-slip wall conditions are applied on the top, bottom, and side boundaries to represent the experimental channel section. Finally, no-slip boundary conditions are applied on the surfaces of both hydrofoils.

To ensure the fidelity of the vortex transport and the subsequent inception modeling, we employ an overset grid assembly as shown in Fig. 2. This approach allows for high-density refinement along the predicted vortex trajectories while maintaining high-quality body-fitted cells near the hydrofoil surfaces and the far-field mesh relatively coarser. As shown in the detailed views, the overset overlap region (A) is designed with matching cell sizes across donor/receptor blocks to minimize interpolation errors, while the near-wall region (B) utilizes fine hexahedral layers to resolve the boundary layer.

The overset grid system is composed of four functional blocks: the Primary foil grid, the Secondary foil grid, the refined Wake/Interaction grid, and the Background channel grid. This hierarchy allows for targeted refinement where the SGS model is most active. As shown in Fig. 2, the near-wall regions (B) are resolved with $y^+ < 1$ to accurately capture the initial vortex roll-up. Detailed metrics for these blocks on the Coarse grid are provided in Table 1. Medium and Fine grids are respectively 1.6 and 2.25 times finer than the Coarse grid.

The expansion ratios are strictly controlled, especially in the Wake block (1.10), to minimize numerical dissipation of the tip vortices. By maintaining a high count of cells across the vortex core (see Table 2),

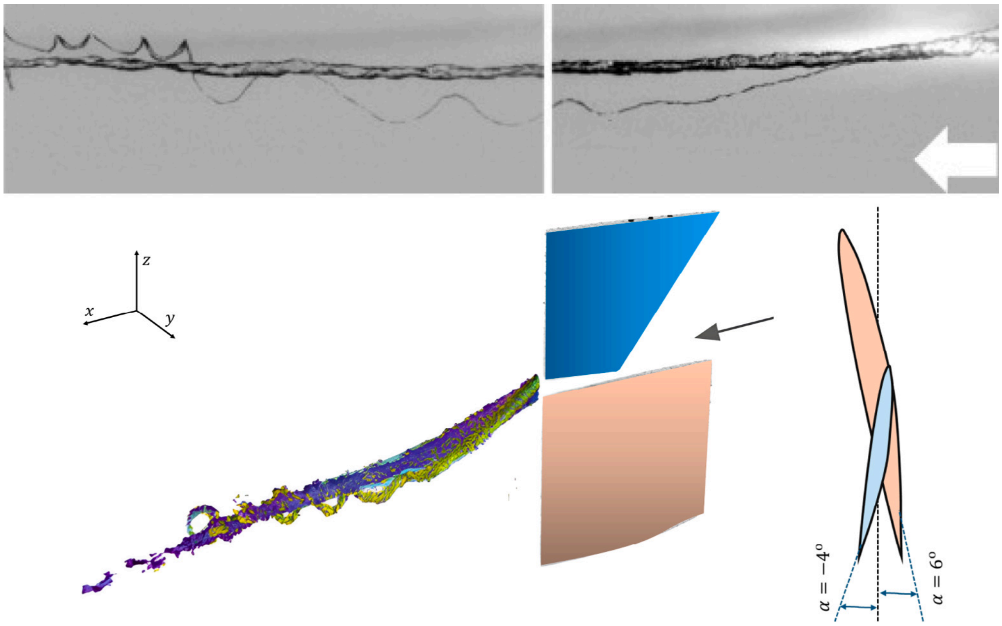

Fig. 1. Numerical setup for the twin hydrofoil configuration. Top: Experimental image showing two initially non-interacting vortices of different strength interacting downstream (From Knister (2024)). Bottom left: Numerical hydrofoils with counter-rotating vortices from one instantaneous flow solution of the medium grid. Bottom right: Schematic of hydrofoil cross sections showing their orientation for N4 case. (For interpretation of the references to color in this figure legend, the reader is referred to the web version of this article.)

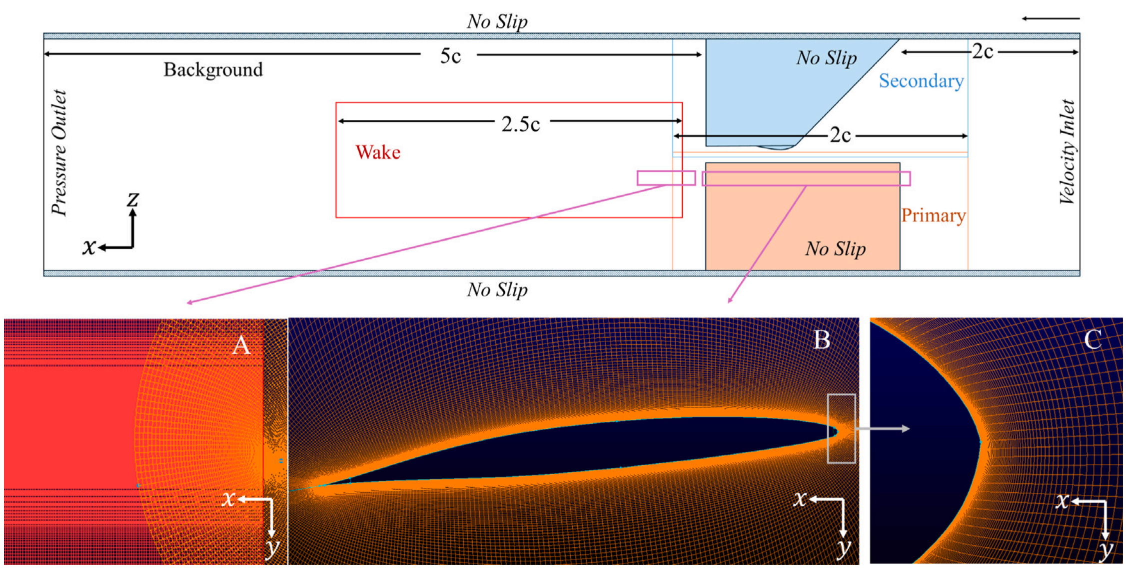

Fig. 2. Schematic of the overset numerical grid setup (top) and detailed local mesh views: (A) Overset overlap region between the wake and primary grid blocks, (B) body-fitted prismatic layers in the near-wall region, and (C) leading-edge refinement on the primary hydrofoil.

Table 1
Quantitative grid metrics for the individual mesh blocks within the overset assembly for the Coarse grid. Hex.: Hexahedral Mesh, Prism.: Prismatic Mesh.

Mesh block	Min. spacing	Expansion ratio	Description	Cell Count ($\times 10^6$)
Primary	2.4×10^{-5}	1.08	Body-fitted, Hex. + Prism.	12.5
Secondary	2.4×10^{-5}	1.08	Body-fitted, Hex.	12.5
Wake	1.0×10^{-4}	1.10	Hex.	65
Background	5.0×10^{-3}	1.20	Hex.	20

Table 2
Spatial & temporal resolution with computational resources used for simulation of each numerical grid.

Grid	Coarse	Medium	Fine
Number of cells ($\times 10^6$)	110	180	250
Cells in vortex core	6	12	25
Timestep ($\times 10^{-4}$)	5	2	1
Number of processors	1250	2070	3072

the LES explicitly resolves the primary pressure drop, while the SGS model identifies the secondary, high-frequency fluctuations that occur at scales smaller than the local spacing.

The meshes are mostly hexahedral but hybrid for Primary hydrofoil block with prismatic layers near the leading and trailing edges. The boundary layers are resolved with a wall-normal distribution ensuring $y^+ < 1$ across all hydrofoil surfaces. By ensuring the boundary layer and initial vortex roll-up are well-captured, the SGS model can accurately target the core regions where sub-grid fluctuations are most critical.

Unless otherwise specified, all the quantities presented are nondimensionalized using the reference chord length c, the reference velocity U_∞, and the reference density ρ. The reference quantities for this configuration are the undisturbed upstream velocity $U_\infty = 10\,\mathrm{m/s}$, the chord length of the primary hydrofoil $c = 0.167\,\mathrm{m}$, and the density of freshwater $\rho = 998\,\mathrm{kg/m^3}$. This yields a chord-based Reynolds number $Re = U_\infty c/\nu \approx 1.67 \times 10^6$.

4. Results

This section presents the key findings of the LES simulations and the application of the SGS cavitation inception model. The results focus on the complex flow structures generated by the interacting hydrofoil wakes, the resulting pressure fluctuations, the characteristics of both resolved and unresolved turbulence, the role of cavitation nuclei, and the predicted cavitation event rates. Comparisons are made to available experimental data and the sensitivity of the predictions to numerical parameters such as grid resolution is investigated.

4.1. Flow field

The formation and downstream evolution of tip vortices are central to the flow physics behind finite-span hydrofoils. Lift generation produces a pressure differential across the hydrofoil surfaces, which, at the spanwise tip, causes concentrated tip vortices whose dynamics govern cavitation inception.

The primary tip vortex, originating from the rectangular hydrofoil, rotates clockwise and maintains a relatively straight trajectory downstream, exhibiting only minor displacement in spanwise and vertical directions from its initial axis. The secondary vortex, shed by the tapered hydrofoil, is counterclockwise, initially angled relative to the primary but quickly realigning parallel by approximately $0.75c$ downstream, with c denoting chord length. The bottom panel of Fig. 1 illustrates these features: low-pressure vortex structures are visualized by an isosurface of nondimensional pressure at -0.12, within which contours of axial vorticity identify the primary (purple) and secondary vortex cores. The secondary begins to develop sinusoidal undulations after $1.0c$ — a signature of Crow instability — which amplify as it wraps around and interacts dynamically with the primary. Ultimately, the secondary vortex undergoes breakdown and fragmentation after about $1.5c$ downstream, indicative of the transition to fully nonlinear mutual distortion and the formation of vortex rings.

These evolutionary stages manifest clearly in both instantaneous and time-averaged velocity and vorticity fields as shown in Fig. 3. For the N0 condition (representing a strongly paired system), the instantaneous axial velocity fields sampled at ten streamwise locations ($x = 1.0, 1.2, \ldots, 2.8$) capture the dynamic interaction and variability of the vortices. Near the hydrofoil trailing edge, both primary and secondary vortices exhibit high axial velocities localized in their cores. As the flow advects downstream, mutual induction and instability processes act to decrease these peak velocities; by about $1.2c$, as the two cores draw closer, axial velocities inside the cores drop below the freestream value, reflecting the impact of interaction and deformation.

The average velocity between the two vortices is consistently lower than the freestream, a direct consequence of their counterrotating arrangement and the induced mean shear between them. This spatial mean illustrates the mean trajectory of each vortex and the instantaneous snapshots reveal higher local intensity and temporal variation.

Table 3
Comparison of instability location, and values of distance between vortices (b), radii of primary and secondary vortices at $x = 1.68$. All quantities are measured similar to Knister (2024).

	$x_{instability}$	b	r_p	r_s	u_p	u_s	ω_{max-p}	ω_{max-s}
Experiment	2.1–2.5	0.103	0.25	0.27	1.28	0.93	11.4	4.8
Coarse	2.0–2.6	0.091	0.28	0.24	1.26	0.89	10.7	5.2
Medium	2.1–2.6	0.097	0.26	0.23	1.26	0.91	10.9	4.9
Fine	2.15–2.65	0.102	0.26	0.22	1.28	0.94	11.3	5.1

Instantaneous axial vorticity fields further show the time-resolved development of the vortex system. Regions of blue in Fig. 3(b) denote primary, clockwise vorticity, and red regions signify the counterclockwise secondary vortex. Initially, the wake is filled with small-scale patches of both vorticity signs, which coalesce and concentrate rapidly along their respective vortex axes as they move downstream. After around $1.0c$ downstream, the vortices mutually interact, stretch, and undergo instability-driven deformation.

The average core radius of the secondary vortex is initially smaller than the primary, grows and becomes nearly equal between $1.2c$-$1.6c$, then thins out beyond this region. The mean vorticity field accordingly shows broader, slightly elongated core regions and smoother gradients, reflective of episodic wandering and stretching observed in the instantaneous data. The meandering of the secondary vortex is particularly significant: averaging over many samples tends to spatially smear the CCW vorticity around the primary, sometimes leading to apparent disappearance of strong CCW signatures after breakup.

The N4 condition, representing a more weakly coupled vortex pair, displays distinctly different behavior in the average fields. The secondary vortex here is initiated at greater distance from the primary, with a smaller initial core radius—an effect of larger hydrofoil AOA. In the average velocity field for N4 (Fig. 3(e)), fluctuations between the two vortices are subdued due to the increased separation distance and reduced mutual induction. The primary vortex remains comparatively unaffected, maintaining a straight trajectory oriented higher ($+z$) and farther spanwise ($-y$) than seen in N0. The corresponding averaged axial vorticity field (Fig. 3(f)) shows a thinner, weaker secondary vortex, which becomes parallel to the primary earlier, and quickly loses coherence after interacting downstream: the instability onset occurs earlier ($\sim 2.0c$), and the secondary breaks up more rapidly.

Note how instantaneous snapshots capture the true intensity and compactness of the vortex cores, as well as episodic phenomena such as local stretching, low-pressure events, and moments of core breakup. Mean fields provide persistent vortex trajectories and statistically dominant features, but are inherently limited by vortex wandering and temporal variability—features which broaden the apparent core size and reduce peak vorticity. The limitations of using mean fields to characterize the vortex properties are particularly pronounced during episodes of strong instability.

Validating key vortex parameters such as instability location, intervortex distance (b), and core radii (r_p, r_s) against experiments reveals consistent agreement across grid resolutions; the LES results align within a few percent of measured values, as shown in Table 3, with the onset of instability ranging from $2.1c$ to $2.65c$.

This agreement across the three grids confirms that the mesh sufficiently resolves the global vortex features, specifically the size, location, velocity, and vorticity distribution. However, while the global flow is well-resolved, large SGS corrections are physically necessary to recover the rare, intense pressure dips ($>30\rho u'^2_{\mathrm{sgs}}$) that are inherently filtered out of the resolved pressure field ($\overline{p}$). Although these extreme pressure excursions do not affect the macroscopic trajectory of the vortices, they are the primary drivers for cavitation inception.

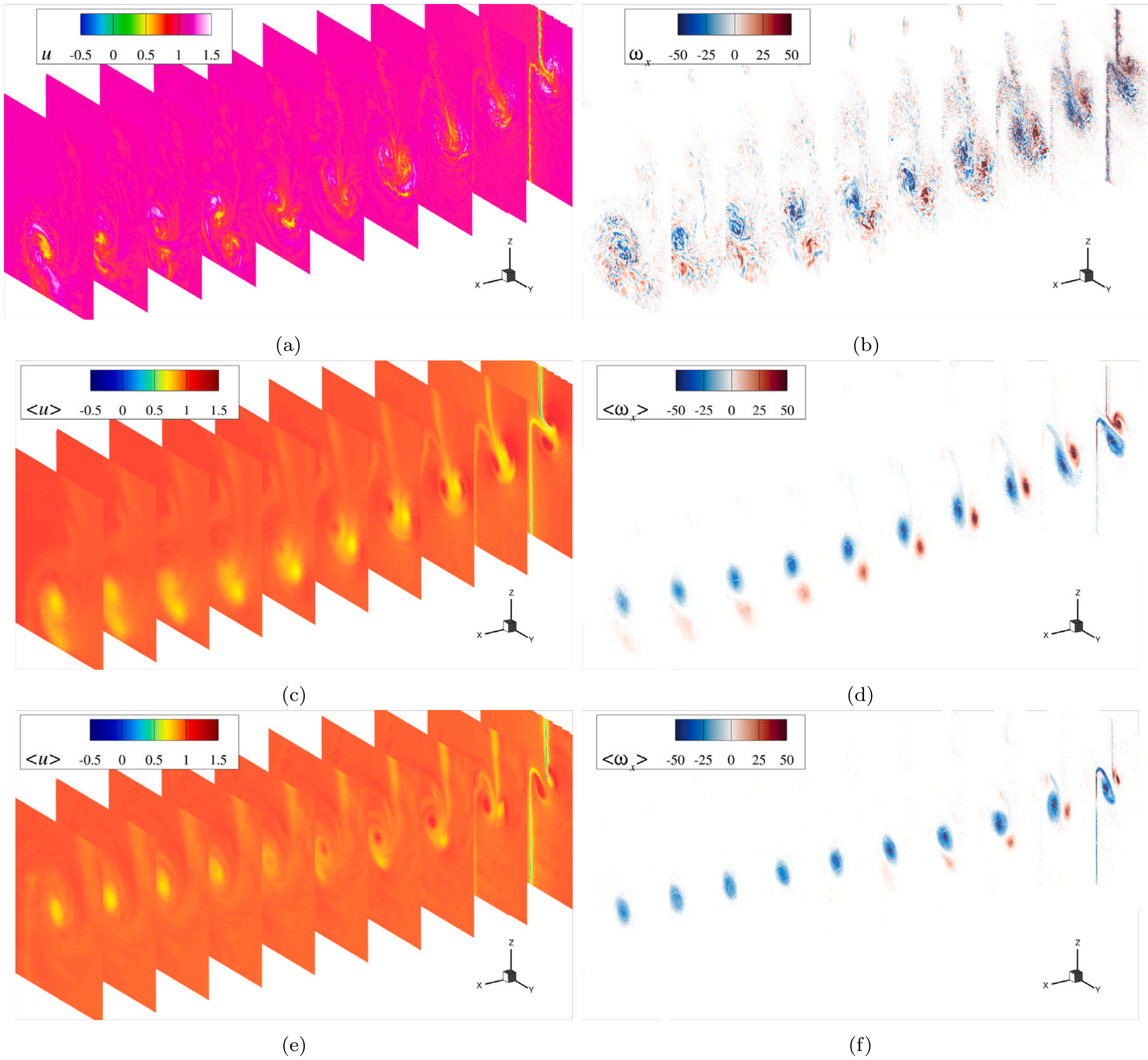

Fig. 3. Contour plots of an instantaneous streamwise velocity (a), instantaneous streamwise vorticity (b), time averaged streamwise velocity (c), and time averaged streamwise vorticity illustrating the overall axial and rotational flow pattern across stations at different downstream locations in the wake of the hydrofoils of N0 condition with medium grid. Time averaged streamwise velocity (e) and vorticity (f) of N4 condition with medium grid. (For interpretation of the references to color in this figure legend, the reader is referred to the web version of this article.)

4.2. Resolved pressure field and fluctuations

The three-dimensional pressure field (Fig. 4) resolved in the LES offers a view of vortex-core evolution and interaction, highlighting regions of potential cavitation and the transient nature of low-pressure phenomena. The instantaneous pressure field for the N0 condition (Fig. 4(a), corresponding to the same instant as Fig. 3(a)) reveals how initially the secondary vortex presents a pronounced low-pressure core near the trailing edge, resulting from strong rotational motion; as the flow convects downstream and the secondary vortex core narrows due to stretching and Crow instability, its core pressure gradually increases. Conversely, the primary vortex exhibits its lowest pressure near $1.5c$ downstream, coinciding with the point of maximum core coherence and strength. These extreme pressure drops are frequently localized within the secondary vortex as it is stretched and entrained by the dominant flow of the primary, underlining its susceptibility to cavitation inception.

Three-dimensional isosurfaces of pressure at $\overline{p} = -0.12$, shown in Fig. 4(b), clarify the structure and mutual interaction of the vortex system, mapping the pressure-based cores of both vortices and visualizing the zones most vulnerable to cavitation. These isosurfaces highlight the dynamic geometry and variation in core size as both vortices destabilize and interact—features central to downstream pressure minima and secondary vortex breakdown.

Pressure fluctuation contours (Fig. 4(c)), depicting the resolved $\overline{p'p'}$ field, further emphasize that the wake is highly unsteady within the vortex cores, where pressure fluctuations can exceed $0.5\rho U_\infty^2$ and abruptly transition to much steadier fields away from the cores. Pressure fluctuations are highly localized to vortex cores and intensify during periods of instability, with rare but significant transient dips serving as precursors for cavitation inception. Both vortex cores contribute strongly to pressure variability, but the highest-amplitude fluctuations and most frequent excursions are typically associated with the more deformable secondary vortex, especially during periods of stretching and reconnection.

Temporal analysis of minimum pressure histories, illustrated in Fig. 5(a) for different grid resolutions and operating conditions, underscores the sensitivity of simulated pressure extremes to both grid resolution and angle of attack. For N0, the coarse grid produces the least fluctuation and the least extreme low pressure, while the fine grid captures deeper and more intermittent pressure drops, with minimum values reaching $-1.25\rho U_\infty^2$. The medium grid yields intermediate results, substantiating the expectation that finer resolution better resolves sharp gradients and low-pressure events. When comparing N0

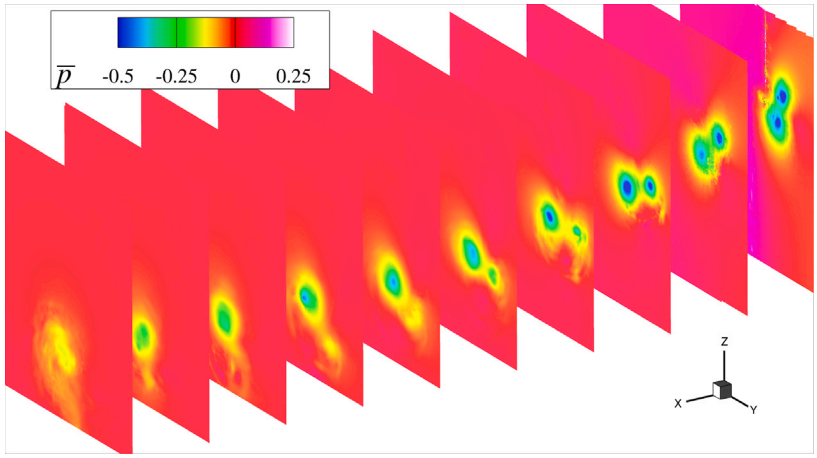

(a)

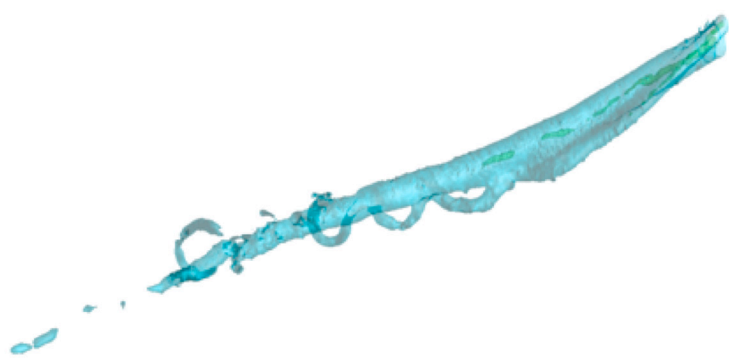

(b)

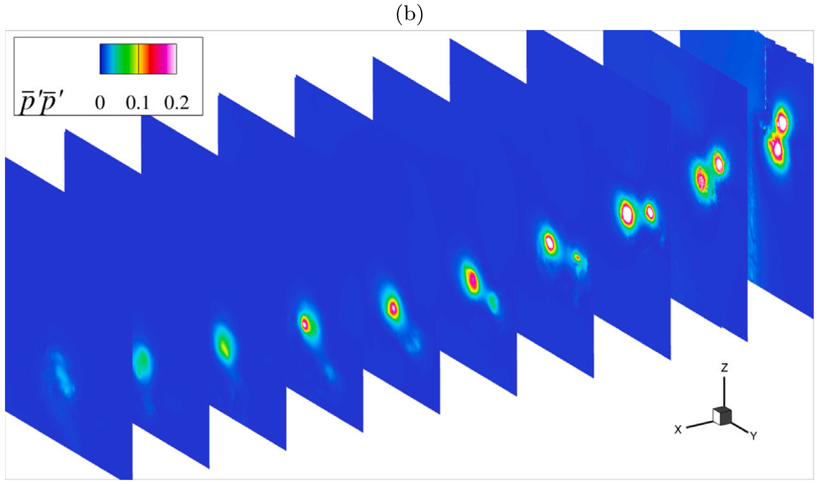

(c)

Fig. 4. (a) Contour plot of instantaneous pressure ($\overline{p}$), showing the spatial distribution of the pressure field downstream of the hydrofoils relative to the reference pressure $\overline{p}_{\mathrm{ref}}$. (b) Isosurfaces of pressure ($\overline{p}$) at −0.12 (Blue) and −0.25 (green) showing the low pressure within the vortices. (c) Instantaneous square pressure fluctuation contours showing concentrated regions of high pressure fluctuations within the vortex cores. All plots correspond to N0. (For interpretation of the references to color in this figure legend, the reader is referred to the web version of this article.)

to N4 for both medium and coarse grids, it is clear that N0 generates significantly lower pressure minima — by approximately $0.3\rho U_\infty^2$ — and exhibits greater intermittency, indicating enhanced instability and vortex interaction at higher circulation. These trends are confirmed by PDFs of pressure (Fig. 5(b)), where the exponential tail for N0 begins to differentiate at $-0.35\rho U_\infty^2$; the fine grid reveals a higher incidence of low-pressure events relative to medium and coarse grids, while N0 consistently presents steeper PDF tails compared to N4, mirroring the observed pressure activity and statistical spread.

Further insight is provided by the PDFs at five streamwise zones downstream of the hydrofoils, as shown in Fig. 5(c). At $x = 1.2$ plane, the highest probability of low-pressure events is found, coinciding with strong rotational vortex cores and maximal pressure depression. The next plane at $x = 1.6$ maintains substantial low-pressure activity,

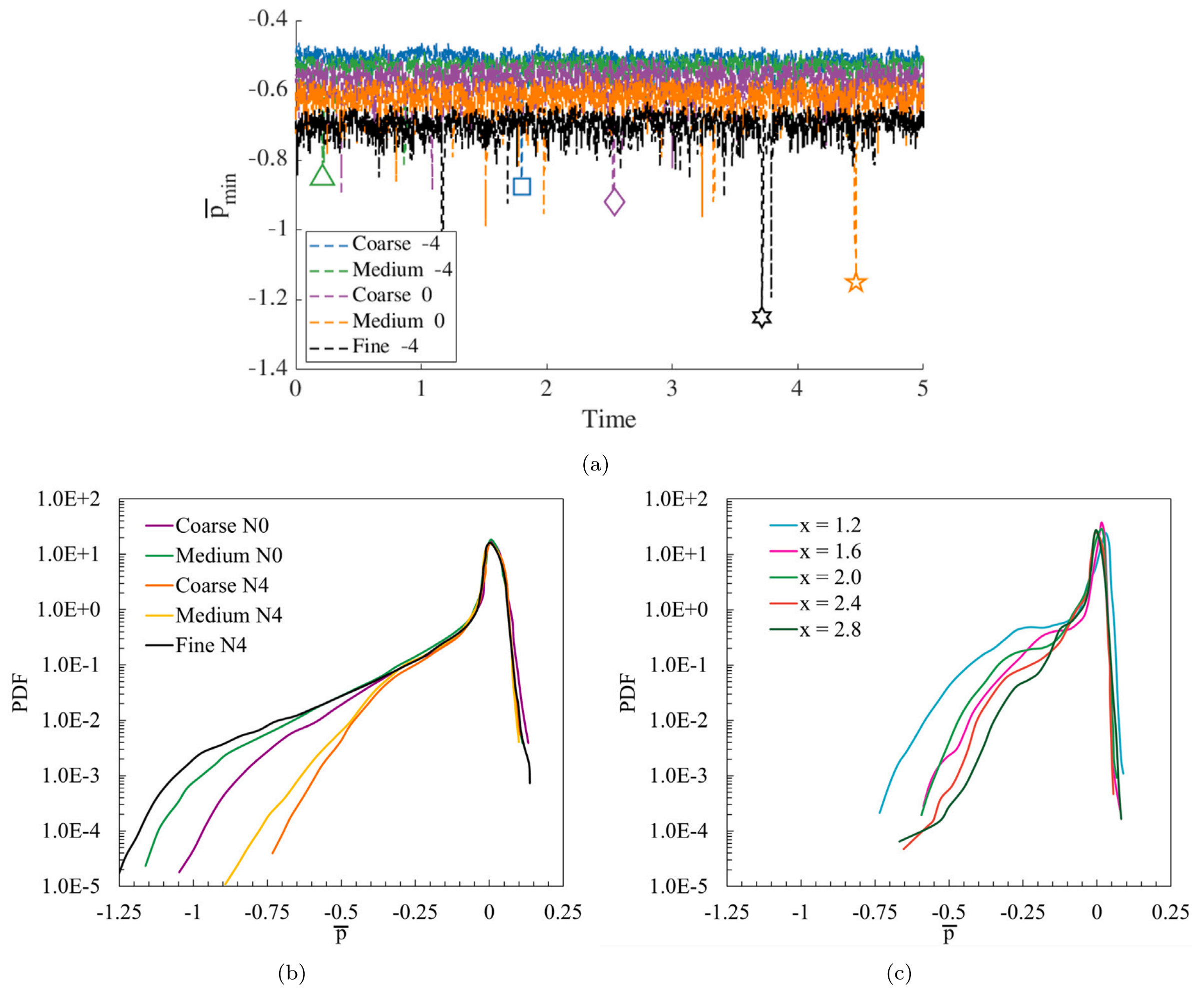

Fig. 5. (a) Minimum pressure histories for N0 and N4 with three grid configurations for a randomly chosen time interval of 5 units, the symbols represent the minimum pressure within the specified time. (b) PDFs of resolved pressure within the specified time for a $(2c, 0.6c, 0.6c)$ sized box centered at $(2.0, 0, 0.9)$. (c) PDFs of resolved pressure at different axial planes downstream of the hydrofoils.

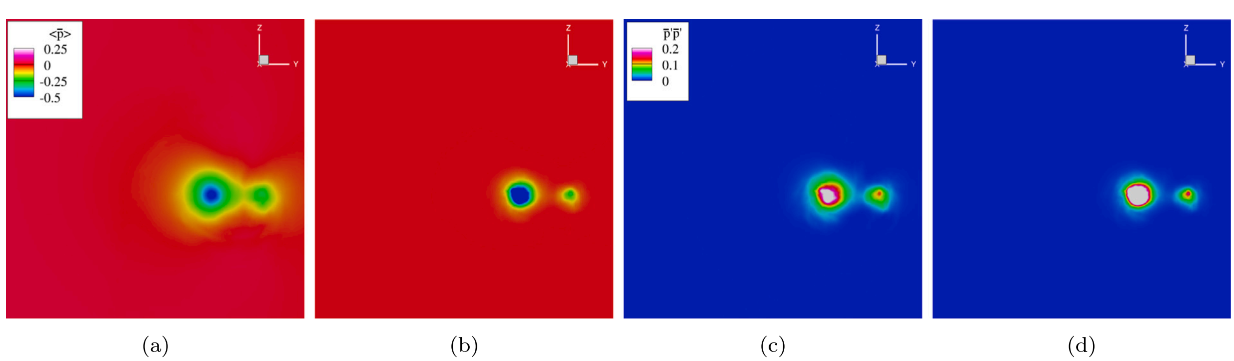

Fig. 6. Grid resolution comparison of pressure for the N0 condition. Time averaged pressure $\langle \overline{p} \rangle$ (a, b) and variance $\overline{p}'\overline{p}'$ (c, d). Panels (a,c) and (b,d) respectively represent the coarse and fine grid results.

primarily attributed to the primary vortex as the secondary core begins to diminish in size and strength. Notably, the two planes at $x = 2.4$ and 2.8 exhibit persistent low-pressure occurrences below $-0.5\rho U_\infty^2$—a phenomenon less apparent in average-field contour plots, but revealed by instantaneous evaluation and the PDFs. These low-pressure events correlate strongly with mutual vortex interaction, periodic stretching, and the onset of Crow instability, which create localized valleys in pressure and enhance the likelihood of cavitation. Across spatial scales, the secondary vortex is consistently a regular site for deep and fluctuating pressure minima, particularly as it interacts dynamically with the primary, although for the coarse grid simulations, they are not enough to predict cavitation inception.

To complement the minimum-pressure histories and PDFs, Fig. 6 compares the mean pressure field and the pressure fluctuation level between the coarse and fine grids for N0 case at $x = 1.6$. The mean pressure panels show that both grids reproduce the same large scale

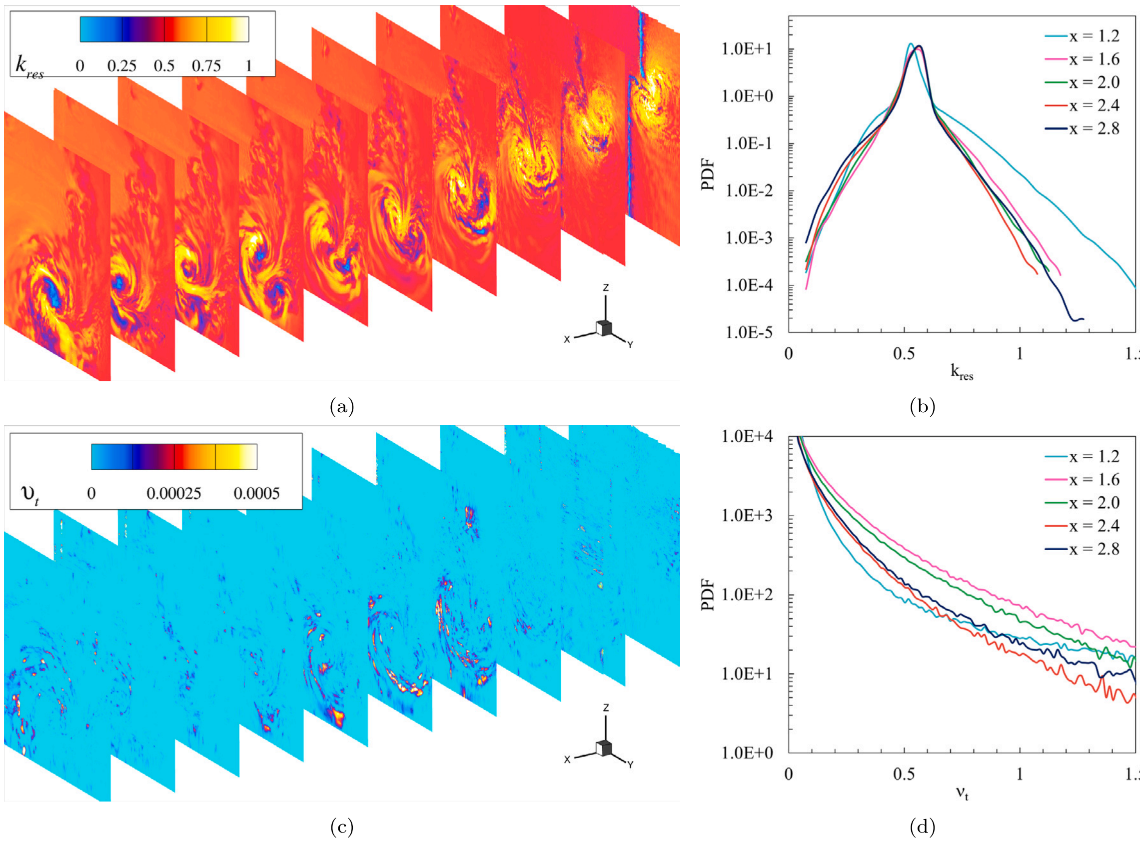

Fig. 7. Contour plots of instantaneous resolved TKE (a) and modeled turbulent eddy viscosity (b), showing the spatial distribution of strong turbulence contained in the resolved turbulent scales.

wake topology and vortex-core locations: the primary and secondary low-pressure regions occur in the same regions downstream, and the overall decay of the pressure deficit with x is similar. The primary differences emerge in the sharpness and compactness of the cores: on the coarse grid, the low pressure cores appear more smeared, with weaker gradients and a broader pressure deficit, whereas on the fine grid the cores are more compact and the mean pressure minima are deeper and more localized. These resolution effects are even more pronounced in the fluctuation panels. The coarse grid substantially attenuates $\overline{p'p'}$ within the vortex cores and yields a more diffuse region of elevated unsteadiness, while the fine grid concentrates $\overline{p'p'}$ tightly within the cores and reveals higher amplitude, more intermittent fluctuations associated with stretching and close vortex–vortex interaction.

4.3. Resolved turbulence

Velocity fluctuations directly drive local pressure depressions that enable nuclei growth. Fig. 7(a) presents contour plots of resolved turbulent kinetic energy (k_{res}), highlighting regions of high velocity fluctuation in the wake. In the near downstream region immediately behind the trailing edge, k_{res} is distributed fairly uniformly both around and inside the tip vortices, indicating a period of active vortex roll-up marked by intense turbulence throughout the wake. Here, the vortices have substantial axial velocity and vorticity, resulting in elevated k_{res} within and nearby the vortex cores. As the vortices advect downstream, their axial momentum decreases and axial velocity fluctuations diminish; this reduces k_{res} inside the cores. However, spanwise and vertical velocity fluctuations persist, especially at the vortex periphery, shifting high k_{res} from the core center to the outer regions and producing localized bands of pronounced turbulence—particularly where vortex interaction and instability amplify velocity gradients.

A statistical perspective is provided by the PDFs of k_{res} across multiple stations downstream, as shown in Fig. 7(b). At all slices, the PDFs retain similar shapes, with lower and upper limits of approximately 0 and 1, and a mean value around 0.55. Notably, the station at $x = 1.2c$ — closest to the trailing edge and depicting the strongest, least-evolved vortices — exhibits the highest average TKE, illustrating the turbulence intensity during initial vortex development. Interestingly, station $x = 2.8c$ shows higher k_{res} than intermediate stations (e.g., $x = 2.4c$), reflecting periods of enhanced vortex–vortex interaction further downstream, as also seen from the stretched/elongated active contours in the corresponding plots.

Fig. 7(c) shows the spatial distribution of modeled eddy viscosity, ν_t. This quantity, derived from the SGS model and dependent on grid resolution, connects directly to the SGS velocity fluctuations (i.e., k_{sgs}). Intense ν_t regions are most pronounced from $x = 1.6c$ onward, appearing primarily around the peripheries of the vortices, especially in the region between the interacting vortex pairs. These high ν_t spots tend to originate near the secondary vortex and follow an elliptical path toward the primary vortex, often concentrated at sites of persistent vortex mutual induction and instability.

Fig. 7(d) displays PDFs of ν_t across the same transverse stations. These, too, show a similar distribution shape with heavy exponential tails indicating a prevalence of rare, intermittent bursts of SGS dissipation. Station $x = 1.6c$ displays the highest peak ν_t, in agreement with the contour maps, while values decrease at farther downstream stations as the flow features become less dominated by unresolved scales. In contrast, station $x = 1.2c$ shows the lowest ν_t overall, consistent with well-resolved flow features and minimized SGS effects immediately post roll-up.

The spatial and statistical coupling between resolved velocity fluctuations (k_{res}), SGS mixing (ν_t), and pressure fluctuations is central to cavitation risk. Regions of high k_{res} or ν_t — whether inside vortex

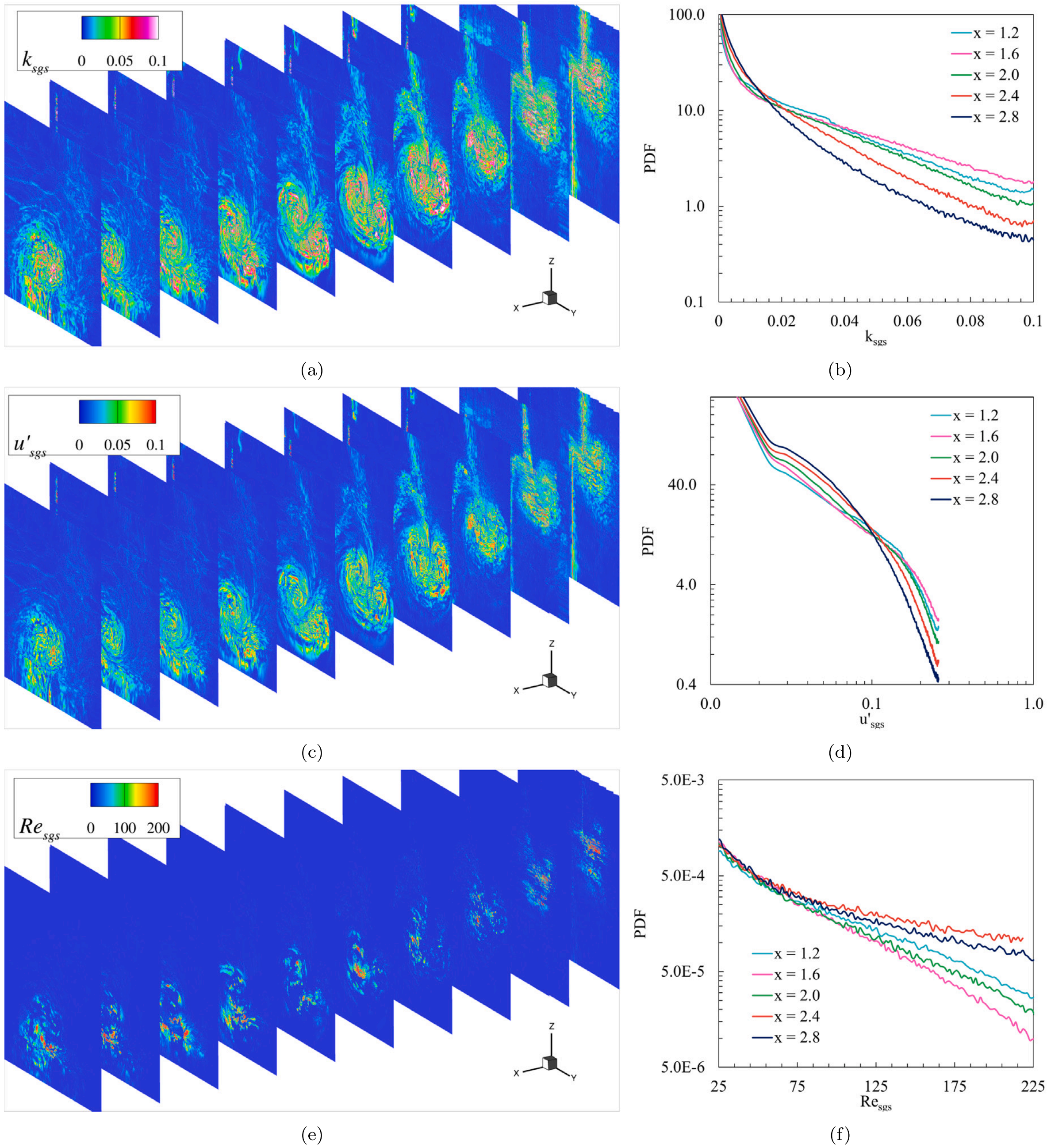

Fig. 8. SGS (a) TKE (k_{sgs}), (b) velocity fluctuation (u'_{sgs}), and (c) Taylor-scale Reynolds number Re_{sgs} at a representative time, indicating the spatial distribution of the unresolved velocity scale and corresponding unresolved turbulence as estimated by the SGS inception model.

cores or at their peripheries — are routinely sites of pronounced instantaneous pressure dips, including the rare negative excursions that drive nucleation. Both metrics are highly intermittent, with spatial and temporal concentration in areas experiencing strong Crow instability oscillations, nonlinear vortex stretching, and mutual reconnection—dynamics as the main drivers of pressure variability and cavitation inception. In particular, the secondary vortex acts as a persistent site for deep and fluctuating pressure minima, as turbulent bursts often originate near and are amplified around its core.

The ability of the LES simulation to resolve these features critically depends on grid fidelity; fine grids capture richer intermittency and more accurate statistics, while coarse grids may underpredict the frequency and severity of turbulence-induced cavitation events.

4.4. Unresolved turbulence

Fig. 8(a) displays contour plots of k_{sgs}, which immediately reveal high SGS turbulence levels in and around the vortex cores in the wake, with concentrations especially prominent around the secondary vortex. As the vortices progress downstream, the spatial distribution of k_{sgs} shifts onto the peripheries—mirroring the patterns found for resolved k_{res} and eddy viscosity ν_t in Fig. 5. In particular, at station $x = 1.6c$ near the secondary vortex core, k_{sgs} attains its peak value; this region, where vortex–vortex proximity triggers primary vortex straining and secondary vortex deformation, is a hot spot for intense turbulence activity. These elevated SGS pockets are highly localized, with k_{sgs} values of 0.05–0.15 remaining prominent at downstream stations, underscoring the spatial intermittency of turbulence in the wake.

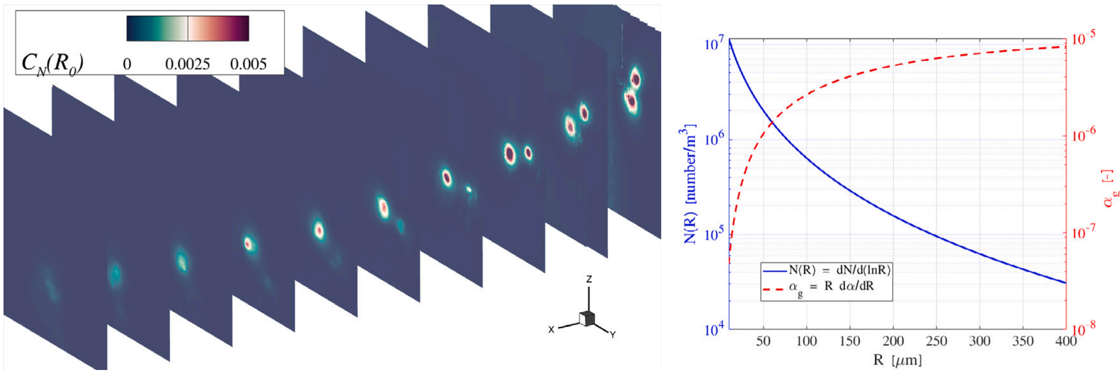

(a) (b)

Fig. 9. (a) Average nuceli concentration $C_N(R_0)$ showing the spatial distribution of bubbles as solved by the vapor transport equation. (b) Initial nuclei size and corresponding vapor volume fraction distribution.

Statistically, the PDFs of k_{sgs} at multiple axial stations, shown in Fig. 8(b), are characterized by exponential distributions consistent with intermittent SGS bursts. The station at $x = 1.6c$ not only exhibits the highest peak values of k_{sgs} but also a broader high-tail distribution, consistent with the regions of strongest vortex interaction and instability identified in the previous resolved turbulence discussion. Other stations exhibit smaller k_{sgs} values as the wake progresses downstream and turbulence intensity generally dissipates.

Fig. 8(c) and (d) illustrate the behavior of unresolved velocity fluctuations, u'_{sgs}. As u'_{sgs} is directly proportional to $\sqrt{k_{sgs}}$, its distribution closely resembles that of k_{sgs}. Displaying u'_{sgs} separately enables direct comparison with the freestream velocity and SGS turbulence via Re_{sgs}. Spatial maps reveal peaks in unresolved velocity fluctuations within wake regions, while the PDFs highlight that rare, intense bursts are concentrated near energetic vortex interactions. Notably, the PDFs of u'_{sgs}, shown on a logarithmic scale, intersect at $u'_{sgs} = 0.1$ for all slices. Moreover, curves with higher probability for $u'_{sgs} < 0.1$ decline more rapidly for $u'_{sgs} > 0.1$, and vice versa.

Fig. 8(c) and (d) further demonstrate this behavior for the unresolved velocity fluctuations; both contour and PDF plots reveal distributions nearly identical to those of k_{sgs}, as these fluctuations are directly linked to SGS energy. The spatial maps locate unresolved velocity fluctuation peaks in the same wake regions, and the PDFs highlight how rare, intense bursts of SGS velocity are most common near energetic vortex interactions.

The SGS Taylor-scale Reynolds number, Re_{sgs}, combines the effects of k_{sgs} and local SGS dissipation (ε_{sgs}). Fig. 8(e), shows high Re_{sgs} values are predominantly concentrated in the region between the vortices and along their peripheries as they move downstream, with markedly higher levels developing around secondary vortex cores at $x > 2.0c$. This spatial variation highlights zones of elevated SGS turbulence where pressure excursions can be magnified and cavitation risk is amplified.

Fig. 8(f) presents the PDFs of Re_{sgs} across axial stations. Most wake regions exhibit low Re_{sgs}, but the probability for intermediate-to-high values ($30 < Re_{sgs} < 200$) remains markedly different for several stations, revealing the persistence of strong subgrid turbulence. The highest probability of extreme Re_{sgs} occurs at $x = 2.6$ (Fig. 8(c)), consistent with high values of both k_{sgs} and resolved turbulence integrated with a slightly larger grid sizes at this location. Furthermore, stations $x = 2.4$ and $x = 2.8$ stand out for their notably higher probability, supporting observations of increased vortex–vortex interaction, turbulence intermittency, and the dynamic migration of hot spots as the vortices evolve downstream.

Relating these SGS patterns to cavitation risk, the localized bursts of k_{sgs}, unresolved velocity, and high Re_{sgs} often coincide with regions of low resolved pressure, especially near vortex interaction sites. According to the SGS inception model, these fluctuations can contribute pressure drops of 10–40 kPa near cavitation nuclei, significant enough to alter inception thresholds estimated by resolved fields alone.

4.5. Nuclei distribution and transport

The spatial distribution and transport of these nuclei within the flow domain significantly influence where and when inception occurs. In complex turbulent flows, nuclei are not passively advected but can be influenced by pressure gradients, turbulent diffusion, and potentially even centripetal forces within vortex cores. In the present study, two modeling strategies were implemented to interrogate nuclei behavior: one assuming uniform, constant nuclei concentration throughout the domain and another employing a dynamic, turbulence-coupled transport model. Both approaches begin with an empirical initial nuclei size and volume fraction distribution, consistent with measurements from typical experimental flows and set to a canonical density of 1×10^7 nuclei/m^3 (Li and Carrica, 2021). This population serves as the baseline for both uniform and dynamic scenarios.

The uniform distribution model treats cavitation nuclei concentration $C_N(R_0)$ and its size spectrum as spatially invariant—every location within the computational domain has the same likelihood of containing nuclei, regardless of flow features or local turbulence. While computationally efficient and serving as a maximum bound for inception probability, this model neglects depletion, enrichment, or clustering effects arising from hydrodynamic interaction and turbulent transport. In such a scenario, cavitation events are distributed exclusively according to pressure minima and do not account for nuclei migration due to evolving turbulent structures and vortex motion. In contrast, the dynamic nuclei model accounts for spatial and temporal variation in nuclei concentrations driven by advection, turbulent diffusion, and source/sink processes. As defined in the scalar transport equation (Eq. (19)), the concentration is locally modulated by D_C, S_e, and S_c. The inclusion of these terms allows the model to capture the reduction of available nuclei in regions of high shear or the enrichment of the wake via surface interactions. Turbulent diffusion is linked to the local SGS kinetic energy and velocity fluctuation magnitude ($D_C \propto \Delta u'_{sgs}$), ensuring that nuclei transport is sensitive to both resolved and unresolved turbulence, and varies in different parts of the flow.

Fig. 9(a) presents the average nuclei concentration $C_N(R_0)$ from the vapor transport model, highlighting regions of nuclei accumulation attributable to modulation by turbulent mixing, and advection with vortical structures. These contour plots reveal that nuclei are especially concentrated within both primary and secondary vortex cores — zones of persistent pressure minima — confirming the physically expected clustering of microbubbles where the conditions for cavitation are most favorable. Note that, while Eq. (19) treats the nuclei density as a scalar field for computational efficiency, the physical effects of force balance

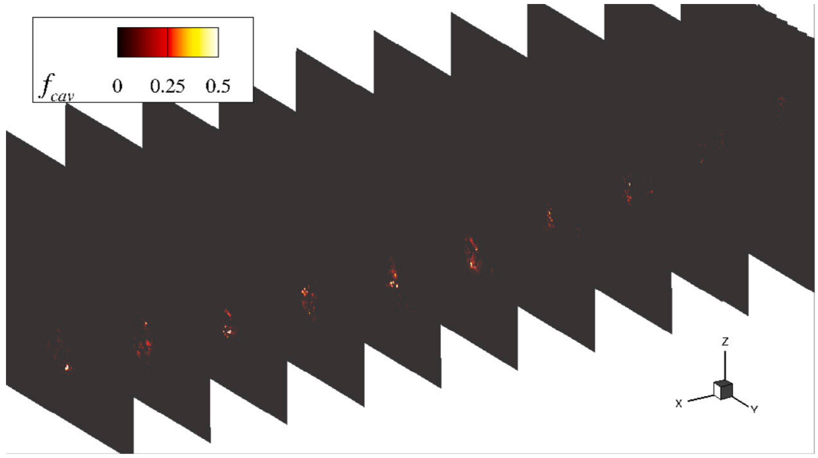

(a)

Fig. 10. Contour plot of the instantaneous cavitation event frequency f_{cav}, showing the locations with high probability of having cavitation inception.

— including drag, added mass, and pressure gradients — are explicitly accounted for within the SGS inception framework. The 4D interpolant database was constructed using bubble dynamics simulations for nuclei in the 20–200 μm range, where these forces are integrated to determine the local event rate. Consequently, the observed accumulation in vortex cores represents a scale-connecting approach: the resolved advection governs global transport, while the force-integrated SGS model captures the pressure-driven trapping physics that leads to localized inception enhancement.

Quantitative analysis of nuclei concentration across the three grids shows that while the global transport patterns are captured on all meshes, the peak concentration within the vortex cores is resolution-dependent. On the fine mesh, the more accurately resolved steep pressure gradients lead to a localized nuclei concentration approximately 15%–20% higher than on the coarse mesh at the same streamwise locations. Streamwise profiles indicate that nuclei concentration remains relatively stable in the primary cores until the onset of Crow instability, where the interaction of the vortices leads to a secondary redistribution of nuclei into the connecting secondary structures.

Spatial and temporal contour mapping of $C_N(R_0, \vec{x}, t)$ illustrates not just nuclei clustering in the wake, but marked heterogeneity and depletion in recirculation zones, shear layers, or regions of high strain. In some cases, nuclei even demonstrate temporal lag in response to rapid pressure transients: their advection and concentration may delay cavitation onset following an abrupt pressure drop, highlighting the importance of coupled transport and mixing in setting the timescale for inception. Specifically, at downstream stations ($x/c > 2.0$), the dynamic model reveals a marked difference in nuclei abundance between the vortex core and the surrounding wake. While the uniform model assumes an identical number of potential sites, the dynamic transport results show that the core can become enriched with nuclei by a factor of 10 or more compared to the ambient fluid, significantly altering the spatial map of potential inception locations.

4.6. Modeled SGS cavitation events

The SGS inception model predicts the volumetric rate of cavitation events (f_{cav}) within the flow by processing the local SGS Taylor-scale Reynolds number (Re_{sgs}), local SGS dissipation rate (ε_{sgs}), local mean pressure (P_0), and the initial nucleus radius (R_0), to determine the probability of a nucleus experiencing a sufficient pressure drop and duration to trigger cavitation.

Fig. 10 presents instantaneous cavitation event rates at different downstream stations, assuming a dynamic nuclei density. These plots reveal that the model predicts higher event rates predominantly in the far-downstream region, where the vortex structures are undergoing intense interaction and breakup. Interestingly, the model does not predict high event rates in the near-downstream of the hydrofoils, despite the presence of relatively low resolved pressures there. Furthermore, the contours clearly indicate that the higher event rates are concentrated within the cores of the secondary vortices, which aligns well with experimental observations of cavitation initiation locations. This spatial agreement provides support for the SGS inception model's ability to utilize the information about unresolved scales and local conditions to identify cavitation hotspots.

The instantaneous cavitation event rates can be averaged spatially and temporally at different reference pressures to generate a cavitation event rate curve, as shown in Fig. 11. Note that, the extent of averaging location is between $0.8c$ and $2.0c$ in the streamwise direction. This domain is chosen to correspond with the region of intense vortex–vortex interaction and secondary filament formation observed in both the current simulations and the experimental visualizations. Because inception in this flow regime is a global phenomenon rather than a localized point-event, a volume-integrated approach is physically consistent with experimental measurement techniques that define inception based on observable events within the wake.

Fig. 11 plots $\overline{F}_{\text{cav}}$ against the reference pressure and provides a means to compare the simulation results with experimental data, which often report cavitation event frequency as a function of test section pressure. To translate these predicted event rates into an inception pressure comparable to experimental observations, we employ two detection thresholds, f_{det}. A threshold of 0.1 Hz is utilized to represent the visual inception limit, where bubbles are produced frequently enough to be perceptible under standard experimental exposure times (Straka et al., 2010; Bappy et al., 2022). Also, a 0.001 Hz threshold is used to denote acoustic events, which typically occur at frequencies significantly lower ($\approx 1/50$–$1/300$) than the visual threshold but are representative of the earliest detectable acoustic signatures (Bappy et al., 2022). For experimental data, we consider cavitation inception when the secondary inception event rate reaches 0.1 Hz (Knister, 2024). As shown in Fig. 10 and Table 4, the $\overline{F}_{\text{cav}}$ curves are remarkably steep in the inception regime. A 3–4 order-of-magnitude variation in f_{det} results in only a minor shift (approximately 10 kPa) in the predicted reference pressure p_{ref}. Furthermore, the functional dependence of $\overline{F}_{\text{cav}}$ on p_{ref} remains invariant across different flow conditions (see Fig. 12). This demonstrates that the model's predicted inception pressure is highly robust; a change in f_{det} effectively corresponds to a minor shift in the definition of an 'observable' event.

The curves in Fig. 11 indicate that small cavitation activities are predicted even at relatively high reference pressures, such as 150 –

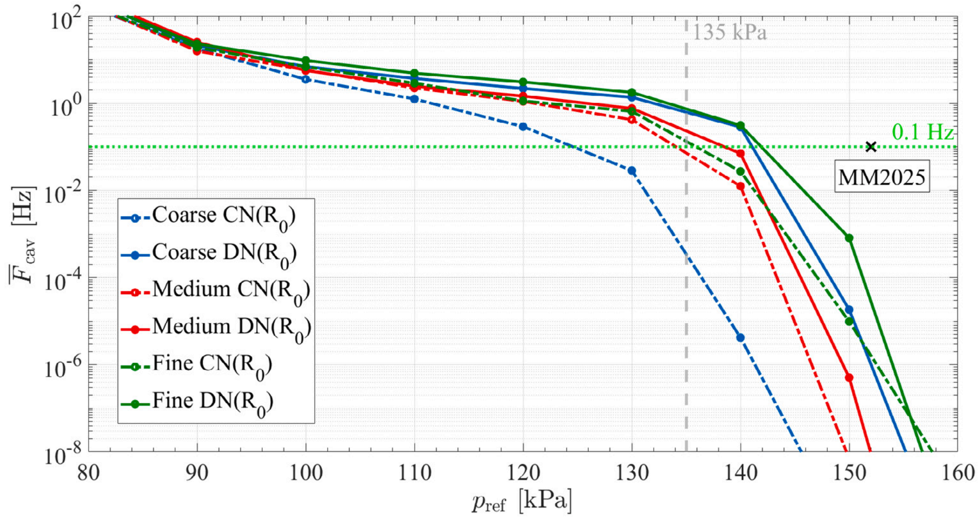

Fig. 11. Average cavitation event frequency for Medium & Coarse grids with and without the dynamic nuclei size distribution. MM2025: (Madabhushi and Mahesh, 2026).

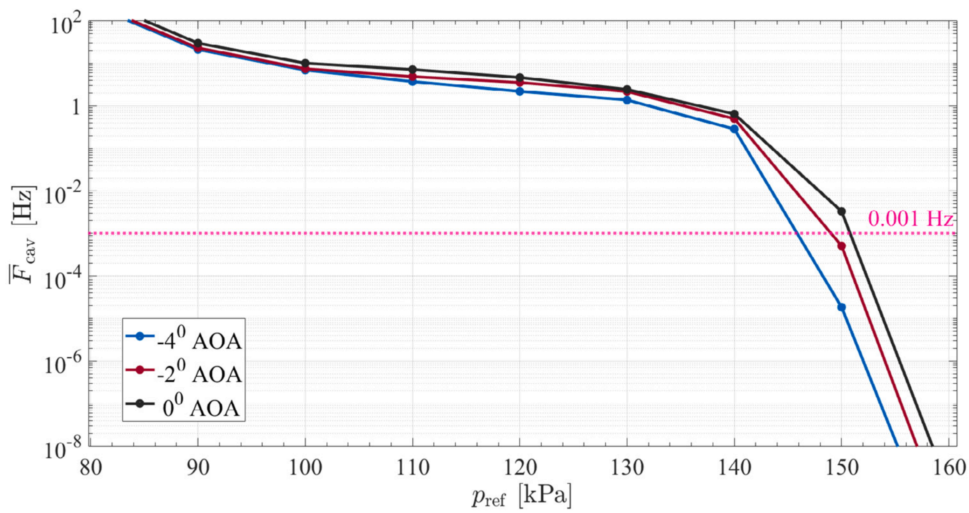

Fig. 12. Average cavitation event frequency for different AOA with the dynamic nuclei size distribution.

Table 4
Inception pressure as predicted by LES and the inception model (with and without dynamic nuclei distributions) at different grid resolutions for −4° AOA. Values are in kPa.

	Resolved LES	$CN(R_0)$	$DN(R_0)$ 0.1 Hz	$DN(R_0)$ 0.001 Hz
Coarse	80.41	123.07	141.24	146.4
Medium	93.35	134.33	138.39	144.15
Fine	127.82	135.58	142.87	149.21
Madabhushi and Mahesh (2026)[a]	152.83	–	–	–

[a] Madabhushi and Mahesh (2026) had a different AOA of −1.5°.

Table 5
Inception pressure as predicted by LES and the inception model (with dynamic nuclei distributions) at different AOAs for the coarse grid. Values are in kPa.

AOA	Resolved LES	$DN(R_0)$: 0.001 Hz	Experimental (Low-High DO)
0°	105.13	150.95	162[a]
−2°	99.53	148.71	142–160
−4°	97.29	146.4	135–155

[a] No high DO data was available.

155 kPa. This is particularly notable considering that the local resolved minimum pressure based inception pressure might only reach around 127.82 kPa even for the finest grid. The ability of the SGS model to predict inception at higher reference pressures is a direct consequence of accounting for the additional pressure fluctuations induced by the unresolved turbulence, which can momentarily drive the total pressure experienced by a nucleus below the vapor pressure even when the resolved pressure is higher. By applying the aforementioned f_{det} thresholds to the curves in Fig. 11, the specific pressure at which the predicted $\overline{F}_{\mathrm{cav}}$ crosses these detection limits can be identified as the numerical inception pressure. The time-averaged f_{cav} contours also suggest strong cavitation activity localized between $1.2c$ and $1.8c$ downstream of the hydrofoils (where c is the hydrofoil chord length), which is consistent with experimental observations of the primary cavitation zone. Therefore, both the predicted inception pressure (as indicated by the onset of significant event rates on the curves) and the spatial location of inception show reasonable agreement with experimental data (see Tables 4 and 5).

4.7. Effect of grid resolution and nuclei distribution

Our results, supported by the findings of Madabhushi and Mahesh (2026), highlight the limitations of using only the minimum resolved pressure (p_{min}) as a criterion for inception. On coarse grids (e.g., −4° AOA), predicted inception pressures based on resolved $\bar{p}_{min}$ are as low as 80.41 kPa, dramatically below the experimentally observed range. Even with our finest grid, the minimum resolved pressure rises only to 127.82 kPa — still notably under the experimental inception threshold of approximately 135–155 kPa. In contrast, Madabhushi and Mahesh (2026), using an exceptionally fine LES grid and Dynamic Smagorinksy (*DSM*) SGS model, reported an inception pressure near 152.83 kPa at −1.5° AOA, which closely matches the experimental results.

With SGS effects included, the proposed statistical inception framework yields a marked improvement in inception prediction even on the coarse and medium grids. With a constant nuclei distribution, $CN(R_0)$, the predicted inception pressures increase to 123.07 kPa (coarse) and 134.33 kPa (medium), capturing a major portion of the gap between resolved-LES-only predictions and experiment. The remaining discrepancies across grids are primarily attributable to the inherent spatial filtering of LES. As established by Madabhushi and Mahesh (2026), capturing the extreme instantaneous pressure minima in these vortices requires grid densities far exceeding typical engineering LES; accordingly, the resolved pressure field (and quantities derived from it, such as $\bar{p}_{min}$) remains grid dependent. Importantly, the SGS inception model does not modify the LES-resolved pressure field; rather, it augments inception prediction by accounting for unresolved pressure excursions statistically. The role of the proposed framework is therefore not to predict the mean or resolved pressure, but to incorporate the influence of unresolved fluctuations parameterized by local SGS turbulence quantities (e.g., k_{sgs}) on the inception event rate. This is reflected in Table 4, where the resolved LES (without the inception model) does not reach inception on any grid, while the model-enabled predictions align closely with the experimentally observed inception range by incorporating the subgrid-scale effects in the inception evaluation.

Predictive fidelity is further enhanced by the dynamic nuclei transport model ($DN(R_0)$). The quantitative impact of this transport is demonstrated in Table 4, where the inclusion of nuclei redistribution and SGS centripetal clustering shifts predicted inception pressures significantly closer to the experimental window. Notably, the dynamic nuclei model demonstrates a reduced sensitivity to grid resolution; while the resolved LES pressure varies by nearly 60% between the coarse and fine meshes, the dynamic nuclei framework maintains a consistent prediction within a narrow 5–8 kPa band. This confirms that inception is heavily modulated by the local availability of nuclei, which cluster in the vortex cores where inception is physically most likely.

With this integrated modeling approach, the predicted inception pressures, with f_{det} of 0.1 and 0.001 Hz, increase to 141.24 kPa and 146.4 kPa, respectively, on the coarse grid. On the medium grid, it increases to 138.39 kPa and 144.15 kPa. Fine grid results show further convergence with the experimental window, reaching 142.87 kPa and 149.21 kPa. For comparison, Madabhushi and Mahesh (2026)'s highly-resolved result of 152.83 kPa (for −1.5° AOA) agrees with the physical upper bound for inception pressure. All model predictions for representative acoustic detection ($f_{\mathrm{det}} = 0.001$ Hz) cluster tightly within the experimentally measured inception range of 135–155 kPa. This threshold represents rare, intermittent events that occur at frequencies approximately 100 times higher than macroscopic, visual events ($f_{\mathrm{det}} =$ 0.1 Hz), making it a more representative indicator for the earliest stages of inception.

4.8. Effect of angle of attack

AOA directly influences the characteristics of the vortices shed from hydrofoils. For a single hydrofoil, increasing the AOA generally increases the lift, producing stronger vortices with greater circulation and greater susceptibility to cavitation inception.

In a twin hydrofoil configuration, the interaction between the two vortices is a complex, three-dimensional process that is highly dependent on their initial strength, size, and relative positions. As the angle of attack becomes more negative, there becomes a larger initial separation between the two vortices. While this greater distance may initially seem to imply a weaker interaction, it also provides a longer streamwise distance for the Crow instability to develop. This extended evolution allows for a more prolonged and intense process of vortex stretching and tilting, which significantly amplifies the vorticity and causes a dramatic reduction in core pressure.

The effect of AOA was assessed only using the Coarse grid. Table 5 outlines how cavitation inception pressure changes with the AOA. With resolved pressure from LES, AOA of 0° gives the maximum inception pressure while AOA of −4° gives the minimum inception pressure. This behavior is quantitatively captured in the cavitation event frequency curves shown in Fig. 12. The curves illustrate that for a given reference pressure, the 0° AOA case consistently yields a higher total event rate ($\overline{F}_{cav}$) compared to more negative angles. As the reference pressure decreases, the growth of event rates for 0° AOA is more rapid, indicating a higher sensitivity to pressure drops in the stronger, more closely spaced vortices produced at lower negative angles.

Fig. 12 shows how the SGS inception model differentiates between these flow regimes. At higher reference pressures (e.g., 160 kPa), only the 0° AOA case shows non-negligible activity, while the −4° case requires a lower system pressure to trigger significant inception. This shift in the curves directly translates to the inception pressure values compiled in Table 5, which show that the trend is in strong agreement with experimental observations. Higher inception pressures under conditions that lead to more vigorous vortex interactions are predicted accurately by the SGS inception model with dynamic nuclei distributions.

It predicts a continuous increase in inception pressure as the AOA becomes more negative. For the $f_{\mathrm{det}} = 0.001$ Hz criterion, it corrects for more than 60 kPa in the SGS, from an inception pressure with resolved LES of 80.41 kPa to 146.4 kPa at −4° AOA. Similar trends are observed for the −2° and 0° AOA with the model predicted inception pressure of 148.71 and 150.95 kPa, respectively.

4.9. Dynamic k_{sgs} model effects

Two contrasting SGS closure models are compared: the algebraic *DSM* and the more advanced *DkM* (Chai and Mahesh, 2012), evaluated with the Fine grid at N0 condition. Both models govern the production, dissipation, and turbulent transport of k_{sgs}, which shape the occurrence and frequency of turbulence-induced cavitation events. The DSM computes the SGS eddy viscosity using an algebraic relation, $\nu_t = (C_s \Delta)^2 |\bar{S}|$, with C_s determined dynamically from local flow properties. In contrast, the DkM model defines $\nu_t = C_s \bar{\rho} \Delta \sqrt{k_{\mathrm{sgs}}}$ and solves an explicit transport equation for k_{sgs}, enabling dynamic closure of all relevant terms and providing enhanced accuracy in representing localized energy transfer and dissipation.

Fig. 13(a) presents time histories of maximum k_{sgs} over a representative unit time in each model. It is immediately clear that the *DkM* sustains significantly higher k_{sgs} and substantially greater intermittency than *DSM*, which produces smoother, less intense fluctuations. This is attributable to the *DkM*'s dynamic closure, allowing for local adjustment of dissipation and turbulence coefficients, which enables k_{sgs} production, transport, and dissipation to be dynamically balanced amid intermittent turbulence. *DSM*, relying on algebraic eddy viscosity damping proportional to resolved strain, artificially suppresses such excursions, resulting in lower k_{sgs} and more monotonic temporal behavior.

This difference in SGS energy translates directly to pressure field behavior, as shown in Fig. 13(b), which displays the time histories of minimum resolved pressure within the analysis window $x = 1.0c$ to $3.0c$. Once again, *DkM* exhibits stronger intermittency and achieves

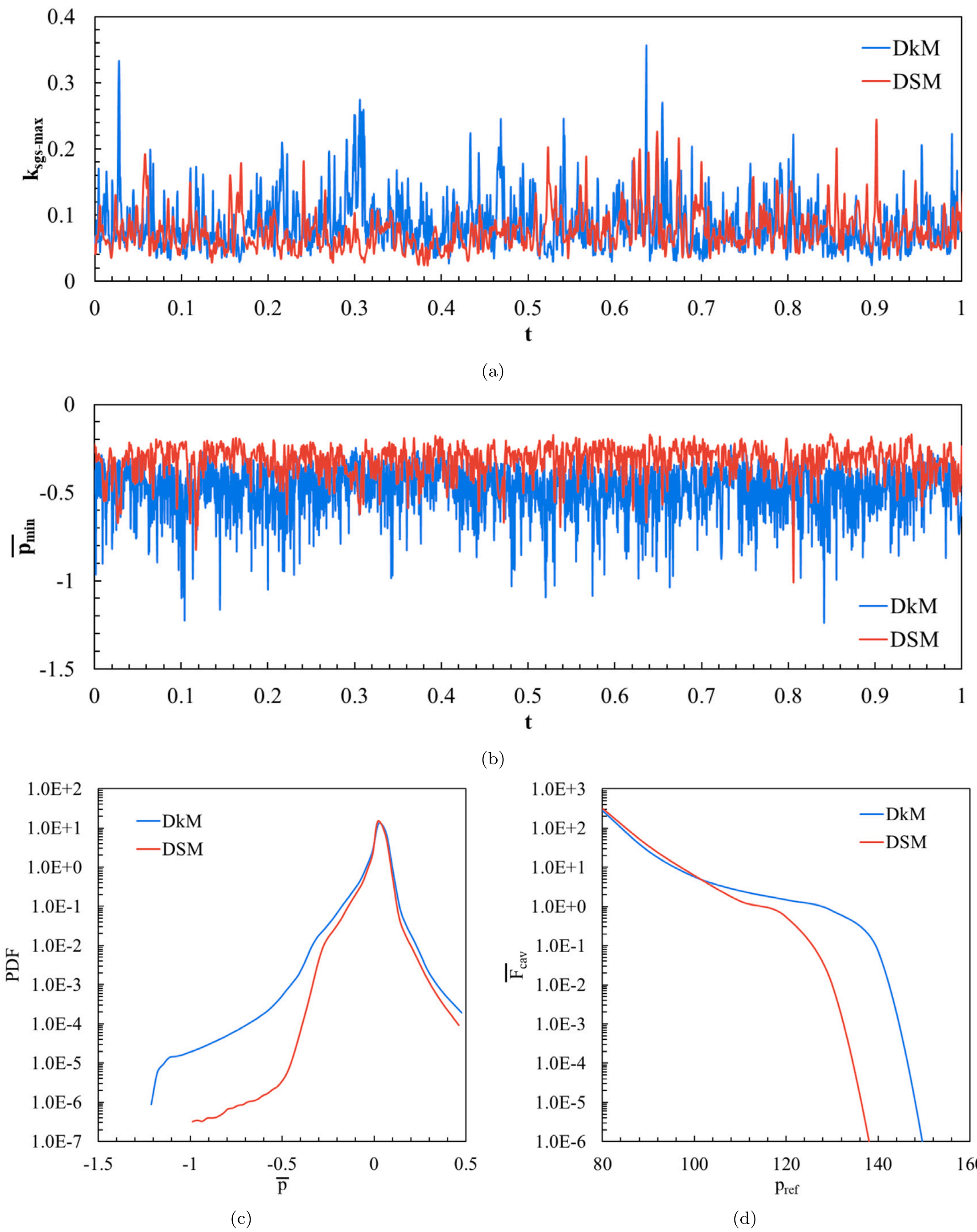

Fig. 13. Time histories of (a) maximum resolved TKE and (b) minimum pressure with *DSM* and *DkM* models for a fine grid 0° AOA case. (c) PDFs of corresponding resolved pressure within the region of interest. (d) Average frequency of cavitation at different reference pressure for the corresponding time.

lower minimum pressures than *DSM*. The periods of deepest pressure excursions closely track intervals of high k_{sgs}, reinforcing the physical connection between localized turbulence energy and instantaneous pressure dips critical for nuclei growth and cavitation inception.

Fig. 13(c) quantitatively compares PDFs of pressure from the same spatial and temporal domain. Both models yield similar distributions for moderate pressure values ($-0.3 < \overline{p} < 0.3$), but differ significantly in low pressure events and shape of the negative pressure tail. *DSM*'s PDF shows a sharper drop-off at $\overline{p} \approx -0.4$ and only a few rare events extending to $\overline{p} = -1.0$; in contrast, *DkM* produces a broad, continuous exponential tail extending to $\overline{p} = -1.25$, indicating a much higher probability of severe pressure reduction. Notably, *DSM*'s exponential tail exhibits a probability nearly 20 times lower than *DkM* at the extreme of the distribution, illustrating that *DSM* predicts only isolated, rare low-pressure events—whereas *DkM* admits a continuum of pressure fluctuations consistent with a physically intermittent turbulence field.

The direct impact of these SGS modeling differences on cavitation prediction is found in Fig. 13(d), which shows the corresponding average cavitation event frequency curves. For *DSM*, the frequency curve drops abruptly at relatively higher free stream pressures, meaning cavitation onset is suppressed and only becomes probable at lower ambient pressure. *DkM*, in contrast, sustains higher frequency and longer tails, with events beginning at higher free stream pressure for the same flow regime.

5. Summary

Predicting cavitation inception in complex turbulent flows is challenging due to the interaction between coherent vortical structures, unresolved small-scale turbulence, and the evolving distribution of vapor nuclei. Traditional modeling approaches, including Reynolds-averaged and even LES, do not capture the intermittent extreme pressure fluctuations responsible for vapor nucleation or neglect the effects of local nuclei transport and accumulation. This paper develops a LES framework that integrates a dynamic k-equation SGS turbulence closure, a statistical cavitation inception model based on probability of pressure fluctuations, and a dynamic nuclei transport equation. This novel combination captures both the intensity and the statistical frequency of extreme pressure excursions at subgrid scales, while simultaneously tracking the spatially and temporally varying concentration of nuclei that act as cavitation seeds.

The dynamic LES framework is demonstrated in the canonical twin vortex problem - a configuration in which two vortices of differing strengths interact. The model resolves large-scale coherent vortex structures and their interactions, and reconstructs the crucial, unresolved turbulence-driven pressure reductions using SGS statistics. By directly simulating the advection and turbulent dispersion of nuclei, the framework identifies where they cluster within low-pressure vortex cores, which are revealed as focal points for cavitation onset. This approach avoids the limitations associated with uniform nuclei assumptions or minimum-pressure criteria, which often poorly estimate inception thresholds and fail to localize likely event sites.

Model performance was tested using multiple grid resolutions and AOA, both with and without dynamic nuclei distributions. For each case, reference pressures and locations corresponding to cavitation inception were computed. Across a range of practical grid resolutions, the proposed LES approach consistently reproduces experimentally observed inception pressures and event locations. Even when using coarser grids that underestimate the true range of pressure fluctuations, the model estimated the frequency and spatial location of cavitation inception with notable accuracy. The inclusion of a dynamic nuclei transport model adds further fidelity, capturing nuclei accumulation in stretched vortex regions under both turbulent diffusion and local pressure gradients.

CRediT authorship contribution statement

Mehedi H. Bappy: Writing – original draft, Visualization, Validation, Software, Methodology, Investigation, Formal analysis, Data curation, Conceptualization. **Krishnan Mahesh:** Writing – review & editing, Supervision, Resources, Project administration, Investigation, Funding acquisition, Conceptualization.

Declaration of competing interest

The authors declare that they have no known competing financial interests or personal relationships that could have appeared to influence the work reported in this paper.

Acknowledgments

This research was supported by the Center for Naval Research and Education at the University of Michigan funded by ONR Grant N00014-24-1-2013. Computations were performed at DOD HPCMP systems under the Frontier project.

Data availability

Data will be made available on request

References

Bappy, M.H., 2022. Statistical Modeling of Cavitation Inception (Ph.D. thesis). The University of Iowa.
Bappy, M.H., Carrica, P.M., Li, J., Martin, J.E., Vela-Martin, A., Freire, L.S., Buscaglia, G.C., 2022. A sub-grid scale cavitation inception model. Phys. Fluids 34 (3).
Brandao, F.L., Mahesh, K., 2022. Large-eddy simulation of cavitation inception in a shear flow. Int. J. Multiph. Flow 146, 103865.
Brennen, C.E., 2014. Cavitation and Bubble Dynamics. Cambridge University Press.
Chai, X., Mahesh, K., 2012. Dynamic-equation model for large-eddy simulation of compressible flows. J. Fluid Mech. 699, 385–413.
Chang, N.A., Choi, J., Yakushiji, R., Ceccio, S.L., 2012. Cavitation inception during the interaction of a pair of counter-rotating vortices. Phys. Fluids 24 (1).
Cheng, H., Long, X., Ji, B., Peng, X., Farhat, M., 2021. A new Euler-Lagrangian cavitation model for tip-vortex cavitation with the effect of non-condensable gas. Int. J. Multiph. Flow (ISSN: 0301-9322) 134, 103441.
Crow, S.C., 1970. Stability theory for a pair of trailing vortices. AIAA J. 8 (12), 2172–2179.
Germano, M., Piomelli, U., Moin, P., Cabot, W.H., 1991. A dynamic subgrid-scale eddy viscosity model. Phys. Fluids A: Fluid Dyn. 3 (7), 1760–1765.
Gnanaskandan, A., Mahesh, K., 2015. A numerical method to simulate turbulent cavitating flows. Int. J. Multiph. Flow 70, 22–34.
Harvey, E.N., McElroy, W.D., Whiteley, A., 1947. On cavity formation in water. J. Appl. Phys. 18 (2), 162–172.
Horne, W.J., Mahesh, K., 2021. A hardware accelerated unstructured overset method to simulate turbulent fluid flow. J. Comput. Phys. 444, 110574.
Katz, J., 1984. Cavitation phenomena within regions of flow separation. J. Fluid Mech. 140, 397–436.
Knapp, R.T., Daily, J.W., Hammitt, F.G., 1970. Cavitation. McGraw-Hill.
Knister, D., 2024. Experimental Study of Cavitation Inception During Vortex-Vortex Interaction and Investigation of Constrained Volumetric Velocimetry Methods (Ph.D. thesis). The University of Michigan.
Knister, D., Callison, E., Ganesh, H., Ceccio, S.L., 2020. Experimental study of cavitation inception during the interaction of vortices. In: Proc. 33rd Symp. on Naval Hydrodynamics. Osaka, Japan.
Leasca, T.J., Kroll, T.B., Mahesh, K., 2025. Large-eddy simulation of the tip vortex flow in a ducted propulsor. J. Fluid Mech. 1010, A51.
Li, J., Carrica, P.M., 2021. A population balance cavitation model. Int. J. Multiph. Flow 138, 103617.
Lilly, D.K., 1992. A proposed modification of the Germano subgrid-scale closure method. Phys. Fluids A: Fluid Dyn. 4 (3), 633–635.
Madabhushi, A., Mahesh, K., 2026. Cavitation inception mechanisms during the interaction between a pair of counter-rotating vortices. J. Fluid Mech. 1027, A15.
Mathai, V., Lohse, D., Sun, C., 2020. Bubbly and buoyant particle–laden turbulent flows. Annu. Rev. Condens. Matter Phys. 11 (1), 529–559.
Morch, K.A., 2000. Cavitation nuclei and bubble formation—A dynamic liquid-solid interface problem. J. Fluids Eng. 122 (3), 494–498.
Saffman, P.G., 1992. Vortex dynamics. In: Theoretical Approaches to Turbulence. Springer, pp. 263–277.
Smith, T., Grech La Rosa, A., Piggott, G., Gaivota, J., McMorran, S., 2024. An experimental study of underwater radiated noise from a small vessel with damaged and fouled propellers. JASA Express Lett. 4 (12).
Straka, W.A., Meyer, R.S., Fontaine, A.A., Welz, J.P., 2010. Cavitation inception in quiescent and co-flow nozzle jets. J. Hydrodyn. Ser. B 22 (5), 813–819.
Tennekes, H., Lumley, J.L., 1972. A First Course in Turbulence. MIT Press.
Verma, A., Park, N., Mahesh, K., 2013. A hybrid subgrid-scale model constrained by Reynolds stress. Phys. Fluids 25 (11).